

# Transient sheets of field-aligned current observed by DMSP during the main phase of a magnetic superstorm

Cheryl Y. Huang

Institute for Scientific Research, Boston College, Chestnut Hill, Massachusetts, USA

William J. Burke

Space Vehicles Directorate, Air Force Research Laboratory, Hanscom Air Force Base, Massachusetts, USA

**DISTRIBUTION STATEMENT A**  
Approved for Public Release  
Distribution Unlimited

Received 29 May 2003; revised 12 February 2004; accepted 9 March 2004; published 16 June 2004.

[1] During the main phase of the 6 April 2000 magnetic storm with  $Dst \cong -300$  nT, four Defense Meteorological Satellite Program (DMSP) satellites encountered intense sheets of field-aligned currents (FACs). Their magnetic perturbations were  $>1300$  nT, corresponding to integrated currents  $|J_{\parallel}| > 1$  A/m. The FACs appeared in both the evening and dawn magnetic local time sectors. They had relatively fast rise times ( $\sim 5$  min), lasted for  $\sim 0.5$  hours, and were associated with widespread reconfigurations of plasma in the near-Earth magnetotail. The largest magnetic and related electric field perturbations occurred at magnetic latitudes  $<60^\circ$ . Magnetometer measurements from DMSP satellites show repeated episodes of similarly large FACs late in the main phase of this and other superstorms. Poynting flux calculations indicate that a few percent of the total ring current energy is dissipated as Joule heat in the midlatitude ionosphere during each of these events. A survey of ground magnetometers at auroral and middle latitudes found perturbations typically  $<200$  nT, incommensurate with magnetic observations at the altitude of the DMSP satellites. The small ground responses reflect weak ionospheric Hall currents and provide an empirical validation of the theorem derived by Fukushima [1976]. Height-integrated Pedersen conductances ( $\Sigma_P$ ) calculated with observed precipitating electron fluxes have significantly lower values than those estimated from Ohm's law using simultaneously measured electric and magnetic field variations. This discrepancy suggests that under some highly stressed conditions the neglect of contributions from low energy electrons and precipitating ions can lead to serious underestimates of  $\Sigma_P$  and a consequent misunderstanding of the magnetosphere-ionosphere circuit. **INDEX TERMS:** 2409 Ionosphere: Current systems (2708); 2431 Ionosphere: Ionosphere/magnetosphere interactions (2736); 2788 Magnetospheric Physics: Storms and substorms; 2716 Magnetospheric Physics: Energetic particles, precipitating; **KEYWORDS:** field-aligned currents, superstorms, measured conductances, DMSP

**Citation:** Huang, C. Y., and W. J. Burke (2004), Transient sheets of field-aligned current observed by DMSP during the main phase of a magnetic superstorm, *J. Geophys. Res.*, 109, A06303, doi:10.1029/2003JA010067.

## 1. Introduction

[2] We report the first observations of intense ( $\sim 1$  A/m) but transient sheets of field-aligned currents (FACs) that couple the central plasma sheet with the auroral ionosphere near the maximum epochs of magnetic superstorms. Maximum magnetic perturbations associated with the FACs normally develop at middle ( $55^\circ$ – $60^\circ$ ) magnetic latitudes. Our attention was drawn to these phenomena while comparing ground magnetometer responses to measurements by particle and field sensors on Defense Meteorological Satellite Program (DMSP) satellites during a 4-hour period on 6 April 2000. Six empirical aspects of the data appeared to be unusual:

[3] 1. Although four DMSP satellites traversed the FACs at about the same time in the evening and dawn magnetic local time (MLT) sectors, no commensurate magnetic perturbations were detected at ground stations beneath or conjugate to them. This null result was confirmed in a survey of data from many magnetometer stations at auroral and middle latitudes.

[4] 2. Pedersen conductances ( $\Sigma_P$ ) calculated using Ohm's law differed from estimates based on energy fluxes of precipitating electrons.

[5] 3. In the evening sector, precipitating ion fluxes dominate over precipitating electrons during the interval of downward FAC.

[6] 4. As the evening-sector current system decayed, a new upward FAC developed near the equatorward boundary of auroral electron precipitation. Ion fluxes decreased dramatically, suggesting that upward drifting, low-energy electrons then carried the  $\sim 1$  A/m downward current.

[7] 5. A significant fraction of the total ring current energy was dissipated as Joule heat in the midlatitude ionosphere.

[8] 6. Four distinct episodes of intense FACs occurred during the storm's maximum epoch, each following a pseudo-breakup event, apparent in traces of the auroral electrojet (AE) index.

[9] Both individually and collectively, these unusual DMSP observations suggest that under highly stressed conditions, magnetosphere-ionosphere (M-I) coupling proceeds in ways not fully grasped in current models. The purpose of this paper is twofold. First, we describe relevant DMSP measurements in the geophysical context of a severe magnetic storm. Second, we relate DMSP data to the current understanding of M-I coupling derived from theoretical and observational considerations. We thus identify gaps between DMSP observations and existing models as indicators of new paths for future exploration.

[10] From today's perspective it is difficult to realize that the existence of FACs was a hotly contested issue just 30 years ago [Egeland, 1984; Dessler, 1984]. The existence debate effectively ended with publications by Iijima and Potemra [1976, 1978], showing that global distributions of FACs exist and follow relatively simple patterns to which they assigned the durable monikers of Region 1 (R1) and Region 2 (R2). R1 currents are located near the poleward boundary of the auroral oval, flowing into the ionosphere on the dawn side of the auroral oval and out on the dusk side. R2 currents are equatorward of R1 and have opposite polarities, flowing into the ionosphere on the duskside and out on the dawnside.

[11] Two key papers of the FAC debate are particularly relevant to the present study. The first concerns physical requirements/implications for FACs as agents responsible for M-I coupling. Vasyliunas [1970] used force balance and current continuity to show that FACs are consequences of misalignments between plasma pressure gradients and flux-tube volume gradients in the magnetosphere. Ohm's law dictates that FACs control distributions of electric potential in the ionosphere. Indirectly, through magnetic mapping, they also control electric field distributions in the magnetosphere. The second paper concerns ground signatures of FACs. Fukushima [1976] developed a theorem demonstrating that if FACs close through poloidal currents flowing in a uniformly conducting ionosphere, magnetic perturbations at ground level exactly cancel and produce no ground signatures. We refer to this result as Fukushima's theorem.

[12] The Rice Convection Model (RCM) implements Vasyliunas' prescription [Harel et al., 1981]. RCM only simulates the dynamics of the inner magnetosphere, treating R1 currents and coupling to interplanetary space as outside its boundary of concern. It assumes that plasma compresses adiabatically while calculating the growth of the ring current, the formation of R2 currents, and consequent redistributions of electric fields in the ionosphere/inner magnetosphere. However, Erickson and Wolf [1980] pointed out that adiabatic compression leads to insupportably high plasma pressures. Kivelson and Spence [1988] suggested that ion loss via gradient-curvature drift to the magnetopause lowers plasma pressure. Borovsky et al. [1998] empirically demonstrated that significant departure from adiabatic transport occurs at radial distances between 15 and 6.6  $R_E$  in the

magnetotail. They compared several possible mechanisms, concluding that auroral ion precipitation is responsible for a large fraction of the mass loss. We note that a recent RCM simulation of the June 1991 magnetic storm [Garner et al., 2004] reproduced electric field distributions observed by the Combined Release and Radiation Effects Satellite (CRRES) in the inner magnetosphere and DMSP satellites in the ionosphere [Burke et al., 1998]. However, RCM consistently predicted more plasma pressure than was measured in the ring current population [Garner et al., 2004]. While de facto, pressure balance is maintained in the magnetosphere, details concerning how this is achieved remain unclear.

[13] Richmond and Kamide [1988] developed an empirical approach to specify FAC and ionospheric potential distributions that grew into detailed procedures for integrating ground and space data called assimilative mapping of ionospheric electrodynamics (AMIE) [Richmond, 1992]. Magnetic perturbations observed by ground stations at high and middle latitudes are inverted to specify equivalent ionospheric currents. Raeder et al. [2001] argued that translating equivalent currents into realistic electric field estimates requires precise knowledge about the distribution of ionospheric conductances. To varying degrees of success, conductances can be derived from knowledge of solar ultraviolet radiances [Wallis and Budzinski, 1981] and the fluxes of energetic particles precipitating from the magnetosphere [Robinson et al., 1987]. However, Kamide et al. [1981] warned that perturbations produced by FACs and poloidal closing currents exactly cancel on the ground. AMIE is thus vulnerable to underestimating FAC intensities and ionospheric electric fields.

[14] M-I coupling involves exchanges of charged particles as well as electromagnetic energy. The morphologies and origins of energetic particle precipitation into the polar cap and nightside auroral oval are relevant to this report. Winningham and Heikkila [1974] showed that the polar cap is characterized by nearly uniform precipitation of electrons with  $E < 100$  eV, called polar rain. Winningham et al. [1975] distinguished between two types of auroral electron precipitation referred to as boundary plasma sheet (BPS) and central plasma sheet (CPS) precipitation. BPS precipitation occurs in the poleward part of the nightside oval and is highly structured in energy-versus-time spectrograms. CPS precipitation occurs in the equatorward part of the oval and varies slowly with latitude. DeCoster and Frank [1979] used a similar nomenclature to describe magnetospheric populations observed in the "plasma sheet boundary layer" (PSBL) and "central plasma sheet," leading to confusion about relationships between BPS and PSBL. Galperin and Feldstein [1991] showed that the PSBL covered a much narrower range of magnetic latitudes than the BPS. Episodically, DMSP observes PSBL signatures near the poleward boundary of the auroral oval as  $\sim 1^\circ$  wide regions of intense electric fields and velocity-dispersed ion fluxes [Burke et al., 1994].

[15] Recently, Newell et al. [1996] sorted ion and electron fluxes by latitude in the auroral oval and related the boundaries to transitions in the conjugate magnetosphere. This extends work by Gussenhoven et al. [1983] who interpreted the equatorward boundary of auroral electron precipitation as mapping to the zero-energy Alfvén boundary in the magnetosphere. Four of the boundaries designated by

Newell and coworkers are useful here. Proceeding from low to high latitude, these are (1) the equatorward boundary of auroral precipitation B1, equivalent to the instantaneous zero-energy Alfvén boundary, (2) entry into the main plasma sheet B2e, where average electron energies cease to increase with magnetic latitude, (3) the ion isotropy boundary B2i, marking the transition between quasi-dipolar and stretched field lines, and (4) the poleward boundary of the main oval B5.

[16] *Burke et al.* [1998] compared distributions of energetic particles and electric fields observed by CRRES in the inner magnetosphere with those detected by DMSP F8 in the ionosphere during the magnetic superstorm of 4–6 June 1991. In this study the phrase “penetration electric fields” referred to electric fields in the magnetosphere earthward of the electron plasma sheet boundary, which is magnetically conjugate to B1. As the storm’s main phase progressed, B1 moved equatorward and stabilized at  $\sim 53^\circ$  magnetic latitude (MLat). In a dipole mapping this corresponds to  $L \approx 3$ . However, Figure 6 of *Burke et al.* [1998] shows that throughout the main phase CRRES crossed the inner edge of the electron plasma sheet beyond  $L = 6$ . The difference between the dipole and real mapping of B1 is caused by the inflationary effects of the ring current on magnetic fields near the magnetosphere’s equatorial plane [*Tsyganenko and Stern*, 1996].

[17] The following section describes orbital characteristics and scientific payloads of DMSP satellites and the spacecraft-centered coordinate system used for data presentation. Before presenting DMSP observations, we summarize our techniques for extracting M-I coupling parameters from combined particle and field data. The observations section includes an overview of the 6 April 2000 “superstorm,” a term used to describe magnetic disturbances with  $Dst < -200$  nT. A geophysical context for understanding DMSP observations is established through consideration of solar wind and interplanetary magnetic field (IMF) dynamics and geospace responses represented by variations of selected geomagnetic indices and auroral boundaries [*Newell et al.*, 1996]. The rest of the observations section presents the DMSP data required to support the six empirical results enumerated in the introduction. The discussion section addresses (1) some implications of DMSP measurements for understanding the dynamics of plasma pressure distributions in the storm-time magnetosphere, (2) applications of Ohm’s law in the ionosphere, and (3) validation of Fukushima’s theorem.

## 2. Instrumentation

[18] DMSP satellites are three-axis stabilized spacecraft that fly in circular, sun-synchronous, polar (inclination  $98.7^\circ$ ) orbits at an altitude of  $\sim 840$  km. The geographic local times of the orbits are either near the 1800–0600 (F11, F13) or 2100–0900 (F12, 14, 15) local time meridians. Offsets between the geographic and geomagnetic poles allow DMSP satellites to sample wide ranges of magnetic local times over the course of a day. The ascending nodes of DMSP orbits are on the dusk side of the Earth. Thus the satellites move toward the northwest (southeast) in the evening (morning) sector. Each satellite carries a suite of sensors to measure (1) fluxes of auroral particles (Special

Sensor J4, SSJ4) and (2) densities, temperatures, and drift motions of ionospheric ions and electrons (Special Sensor for Ions Electrons and Scintillations, SSIES). All of the satellites except F11 carry magnetometers (Special Sensor for Magnetic Fields, SSM) to monitor perturbations of the Earth’s magnetic field.

[19] Identical SSJ4 sensors are mounted on the top surfaces of DMSP satellites to measure fluxes of down-coming electrons and ions in 19 logarithmically spaced energy steps between approximately 30 eV and 30 keV [*Hardy et al.*, 1984]. A full spectrum is compiled every second. Unfortunately, fluxes of ions with energies below 1 keV are unavailable from the F15 satellite. SSIES consists of spherical Langmuir probes mounted on 0.8 m booms to measure densities and temperatures of ambient electrons, and three different sensors mounted on a conducting plate facing the ram direction. These are (1) ion traps to measure the total ion densities, (2) ion drift meters to measure horizontal ( $V_H$ ) and vertical ( $V_V$ ) cross-track components of plasma drifts, and (3) retarding potential analyzers (RPA) to measure ion temperatures and in-track components of plasma drift  $V_{\parallel}$  [*Rich and Hairston*, 1994]. Shapes of RPA current-voltage sweeps can be used to determine the masses of contributing ion species. Because of relatively small uncertainties about spacecraft potentials, RPA estimates of  $V_{\text{par}}$  often have large error bars and are not used in this study. Although the drift meters measure  $V_H$  six times per second, data are presented here as 4-s averaged values. Problems with a noisy tape recorder limit the usefulness of data from F11.

[20] SSM sensors are triaxial fluxgate magnetometers that are mounted on the bodies of the F12–F14 spacecraft. The magnetometer on F15 is mounted on a 5-m boom, reducing its susceptibility to spacecraft-generated contamination. Magnetic vectors are sampled 12 times per second. One-second average values are calculated as  $\delta \mathbf{B} = \mathbf{B}_{\text{meas}} - \mathbf{B}_{\text{IGRF}}$ , the differences between measured and International Geomagnetic Reference Field (IGRF) values of magnetic fields at the spacecraft locations. Data are presented as  $\delta B_X$ ,  $\delta B_Y$ ,  $\delta B_Z$  in spacecraft-centered coordinates, as illustrated in Figure 1. The X- and Y-axes point toward spacecraft nadir and along the velocity vector, respectively. The Z-axis completes the right-hand system. Figure 1 shows projections onto an invariant latitude-versus-MLT grid of four DMSP trajectories near 2020 UT on 6 April 2000. F13 and F14 (F12 and F15) were moving equatorward in the morning (evening) sector above the northern (southern) ionosphere. The Z-axis generally points in the antisunward direction, as shown in Figure 1. Nearly simultaneous observations from the SSM, SSIES, and SSJ4 sensors on the various DMSP spacecraft help corroborate and interpret electrodynamic measurements in the storm’s main phase.

[21] To assist the interpretation of DMSP measurements we also examined other data sources. These include: (1) interplanetary plasma and magnetic field measurements from the Wind and Advanced Composition Explorer (ACE) satellites, (2) magnetic fields measured at a large number of ground stations distributed around the Earth, and (3) observations of energetic (keV and MeV) particle fluxes by four Los Alamos National Laboratory (LANL) satellites and magnetic field by two Geostationary Operational Environmental Satellite (GOES) satellites at geostationary altitude. The LANL satellites detected fluctuations in keV

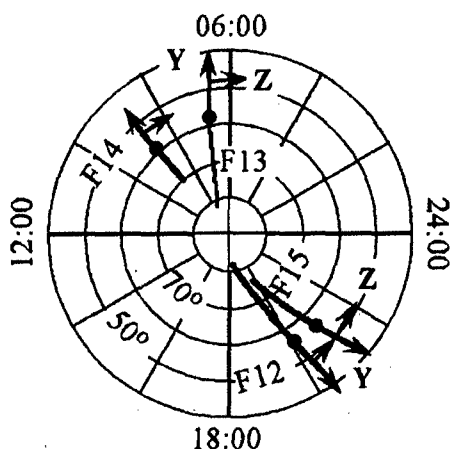


**Figure 1.** Spacecraft-centered coordinate system used to analyze SSM data. Trajectories of four DMSP satellites are projected onto an invariant latitude versus magnetic local time grid. X and Y are directed toward nadir and along the spacecraft velocity vector, respectively. Z generally points toward the antisunward direction. Black circles mark locations on the trajectories where maximum perturbations in  $\delta B_z$  were detected.

particle fluxes that intensified with increased geomagnetic activity. The observed variations showed no obvious correlations with measurements from DMSP or each other. The GOES satellites were both on the dayside during the period of interest and provide no information about nightside electrodynamics.

### 3. Data Analysis Techniques

[22] This paper integrates nearly simultaneous measurements from three sensors on four DMSP satellites to draw inferences about M-I coupling under highly stressed conditions. Techniques used to draw geophysical inferences from the measurements by each sensor are distributed in the literature and are very familiar to specialized analysts. However, it appears useful for the benefit of more general readers to summarize here the analysis techniques and their interrelationships. This section treats characteristics of data streams, in spacecraft-centered coordinates, expected when DMSP satellites cross a pair of quasi-infinite FAC sheets at normal incidence. Methods for identifying breakdowns of the normal incidence and/or infinite current-sheet approximations are briefly indicated.

[23] The two governing equations for analyzing combined SSM and SSIES data are Ampere's law and current continuity:

$$j_{\parallel} = (1/\mu_0)[\nabla \times \delta \mathbf{B}]_{\parallel} \quad (1)$$

$$\partial j_{\parallel} / \partial s = -\nabla_{\perp} \cdot \mathbf{j}_{\perp}, \quad (2)$$

where  $s$  represents an infinitesimal distance along a magnetic field line. In the ionosphere the current density perpendicular to the Earth's magnetic field  $\mathbf{B}_E$  is

$$\mathbf{j}_{\perp} = [\sigma_P \mathbf{E} - \sigma_H (\mathbf{E} \times \mathbf{b})], \quad (3)$$

where  $\sigma_P$  and  $\sigma_H$  are the Pedersen and Hall conductivity, respectively;  $\mathbf{b}$  is a unit vector along  $\mathbf{B}_E$ . Integrating equation (2) from the satellite location to the bottom of the ionosphere gives

$$j_{\parallel} = \nabla_{\perp} \cdot \mathbf{I}_{\perp} = \nabla_{\perp} \cdot [\Sigma_P \mathbf{E} - \Sigma_H (\mathbf{E} \times \mathbf{b})], \quad (4)$$

where  $\Sigma_P$  and  $\Sigma_H$  are the Pedersen and Hall conductances, respectively.

[24] Applied to a DMSP satellite crossing an infinite field-aligned current sheet at normal incidence  $\nabla_{\perp} \rightarrow \partial_Y$ , and equation (1) reduces to

$$j_{\parallel} = (1/\mu_0) [\partial_Y \delta B_z]. \quad (1')$$

By definition, FACs into the ionosphere flow in the +X direction. Equation (1') indicates that in plots of  $\delta B_z$  versus time, FACs into the ionosphere are characterized by positive slopes. Since DMSP satellites move in the +Y direction at speeds of  $\sim 7.5$  km/s, a FAC density of  $1 \mu\text{A}/\text{m}^2$  corresponds to a slope of  $\sim 9.4$  nT/s.

[25] A useful quantity for estimating the total current into or out of the ionosphere is the integrated (A/m) field-aligned current density  $J_{\parallel} = \int j_{\parallel} dY$ . Integration of equation (1') along a trajectory segment gives

$$J_{\parallel} = (1/\mu_0) [\Delta \delta B_z], \quad (5)$$

where the symbol  $\Delta$  represents the difference between  $\delta B_z$  values at the applied limits of integration.  $J_{\parallel} = 1$  A/m corresponds to a magnetic perturbation of 1256 nT.

[26] In our spacecraft-centered coordinate system, equation (4) becomes

$$j_{\parallel} = \partial_Y [\Sigma_P E_Y - \Sigma_H E_Z]. \quad (4')$$

Note that for a normal incidence crossing,  $E_Z$  is the electric field component tangential to the sheet direction. Faraday's law requires that to be constant. Combining equations (1') and (4') gives

$$\partial_Y [\delta B_z - \mu_0 (\Sigma_P E_Y - \Sigma_H E_Z)] = 0. \quad (6)$$

In analyzing combined SSM and SSIES measurements, it is often useful to identify segments in data streams where variations of  $\delta B_z$  and  $E_Y$  are highly correlated. Equation (6) indicates that during such data-acquisition segments the conductance gradients are weak. This judgment can be tested against the properties of particle fluxes measured by the onboard SSJ4 sensor during the same interval [Robinson *et al.*, 1987]. Within the regions of weak conductance gradients

$$\Sigma_P \approx (1/\mu_0) [\Delta \delta B_z / \Delta E_Y]. \quad (7)$$

Our analyses of DMSP measurements also identify particle populations responsible for  $j_{\parallel}$ . SSJ4 sensors monitor ion/electron fluxes moving in the +X direction. Differential fluxes measured by SSJ4 may be integrated over energy (30 eV to 30 keV) to determine number fluxes  $\Phi_{N,s}(\varphi, \psi)$ , in particles per  $(\text{cm}^2 \text{ s sr})$ , for each species,  $s$ . Here  $\varphi$  and

$\psi$  represent the gyrophase and pitch angles, respectively. Assuming that both species are gyrotropic,

$$j_{\parallel} = 2\pi q \int [\Phi_{N,i}(\varphi, \alpha) - \Phi_{N,e}(\varphi, \alpha)] \cos \psi \sin \psi d\psi, \quad (8)$$

where  $q$  represents the elemental unit of charge  $1.62 \times 10^{-19}$  C. Consider a sheet of upward FAC and assume that both precipitating particle distributions are isotropic over the down-coming hemisphere, then

$$j_{\parallel} \approx \pi q [\Phi_{N,i}(\varphi, \alpha) - \Phi_{N,e}(\varphi, \alpha)]. \quad (9)$$

Equation (9) is valid as long as backscattered fluxes are much less than the incident fluxes. Experience teaches that in most geophysical cases upward and downward FACs are carried by electrons moving into and out of the ionosphere, respectively. During the 6 April 2000 magnetic storm, DMSP detected an unusual case in which an intense downward FAC was carried by precipitating energetic ions (empirical result 3).

[27] The final physical quantity used as an analysis tool in this paper is the field-aligned Poynting vector  $S_{\parallel}$  ( $\text{W/m}^2$ ) =  $(1/\mu_0) [\mathbf{E} \times \delta\mathbf{B}]_{\parallel} \approx (E_Y \delta B_Z / \mu_0) \mathbf{x}$ . For reference,  $E_Y$  and  $\delta B_Z$  perturbations of 1 mV/m and 1 nT correspond to  $S_{\parallel} \approx 0.8 \mu\text{W/m}^2$ . On the time scales of interest, Poynting's theorem relates the divergence in  $S_{\parallel}$  to the Joule heat dissipated in the ionosphere beneath the spacecraft

$$\partial S_{\parallel} / \partial s = -\mathbf{j}_{\perp} \cdot \mathbf{E} = -\sigma_P E^2. \quad (10)$$

Integrating equation (10) from the satellite altitude to the bottom of the ionosphere gives  $\Delta S_{\parallel} \approx \Sigma_P E_Y^2$ . The symbol  $\Delta S_{\parallel}$  represents the difference in electromagnetic energy flux carried by incident and reflected Alfvén waves. In the discussion section we show that  $\Delta S_{\parallel}$  is the physical quantity inferred from measured values of  $E_Y$  and  $\delta B_Z$ . Equation (10) thus indicates that the total Joule heat dissipated in the ionosphere can be estimated from combined  $E_Y$  and  $\delta B_Z$  measurements with no prior knowledge of  $\Sigma_P$ . The total rate of electromagnetic energy input to the ionosphere associated with sheets of FAC is

$$\Pi_{\parallel}(\text{W}) \approx \int \Delta S_{\parallel} dY dZ. \quad (11)$$

While we have no direct knowledge of the current sheet's extent in the  $\pm Z$  directions, we can integrate equation (11) numerically along spacecraft trajectories to determine electromagnetic power (and Joule heat) in Watts per meter transferred from the magnetosphere to the ionosphere.

#### 4. Observations

[28] Particle and field measurements by sensors on DMSP provide a rich and complex source for observing electrodynamics of M-I coupling under highly driven conditions. For clarity we divide the observations into four parts. The first subsection contains information about interplanetary drivers and the global geospace response. The latter is manifest through the evolution of standard geomagnetic indices and the movement of auroral boundaries [Newell *et al.*, 1996] during the main phase. The second subsection presents a synopsis of detailed particle

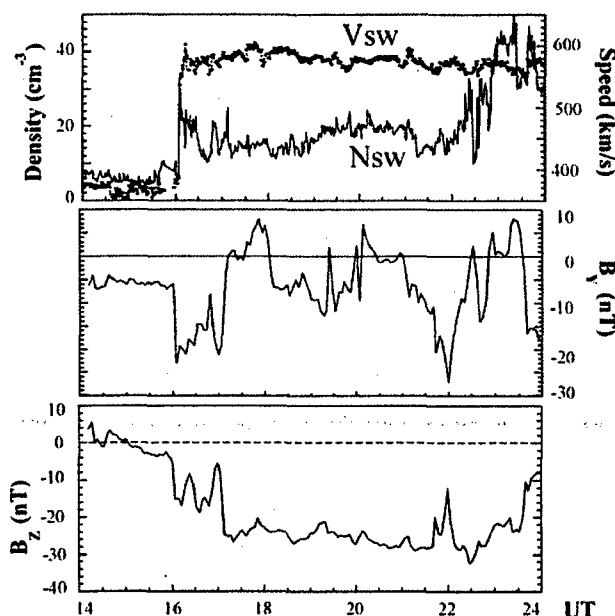


**Figure 2.** The 64-s averaged values of (top) solar wind density (dotted line) and speed (solid line), (middle) IMF  $B_Y$ , and (bottom) IMF  $B_Z$  measured by the ACE satellite near L1 on 6 April 2000.

and field measurements associated with intense FAC sheets. We show an example of FAC pairs dividing into three sheets as they relax toward quiet levels. The third subsection considers circuit impedances estimated from observed fluxes of precipitating electrons [Robinson *et al.*, 1987] and ratios of highly correlated  $E_Y$  and  $\delta B_Z$  variations in equation (7). The  $E_Y$  and  $\delta B_Z$  data are considered from the viewpoint of simple DC circuits and transmission lines. The fourth subsection concerns ground magnetometer measurements taken at the times of the intense FACs.

##### 4.1. Geophysical Background

[29] Partial overviews of interplanetary drivers and of geospace responses during the last 10 hours of 6 April 2000 are provided in Figures 2 and 3, respectively. Figure 2 shows 64 s averaged values of (top) solar wind density and speed, (middle) IMF  $B_Y$ , and (bottom) IMF  $B_Z$  as measured by plasma and magnetic field sensors on the ACE satellite near the first Lagrangian point ( $L_1$ ). These data show that at 1604 UT the solar wind speed increased from  $\sim 400$  km/s to steady values near 575 km/s. At the same time the density rose from 6 to  $20 \text{ cm}^{-3}$ . Near the end of the day, the density rose to  $\sim 40 \text{ cm}^{-3}$ . After 1604 UT the IMF had strongly negative Y and Z components. IMF  $B_X$  (not shown) was near zero all day. The interplanetary shock passed the Wind satellite,  $\sim 55 R_E$  upstream of the Earth, shortly before 1630 UT. Compressional waves caused by the shock's impact on the magnetopause were detected by ground magnetometers at  $\sim 1640$  UT.

[30] Figure 3 shows (top) SYM-H and (bottom) AE indices for 6 April 2000 (available at <http://swdcd.db.kugi.kyoto-u.ac.jp/index.html>). SYM-H summarizes perturbations in the horizontal component of the Earth's magnetic field as measured around the world at midlatitude to low-

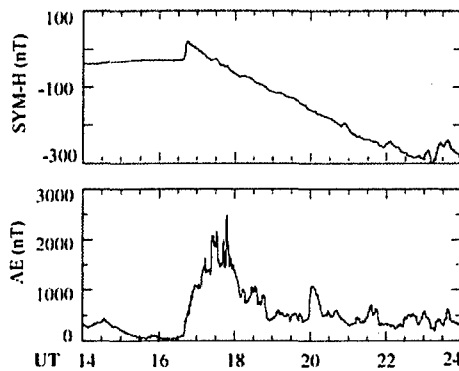


**Figure 3.** One-minute averaged values of the (top) SYM-H and (bottom) auroral electrojet (AE) indices.

latitude stations. Information provided by the SYM-H index is similar to Dst but is presented at a 1-min rather than a 1-hour cadence. Values of the AE index are also presented as 1-min averages. SYM-H rose from  $-27$  to  $+19$  nT between 1640 and 1645 UT, then steadily decreased through the rest of the day to  $\sim -300$  nT as the ring current intensified. Sustained recovery began early on 7 April. The auroral electrojet intensified immediately after the sudden storm commencement (SSC) event. Activity was sporadic, three times exceeding 2000 nT before declining after 1750 UT. A 10-min auroral activation began at 2000 UT, with AE reaching 1085 nT. This excursion was dominated by much larger contributions from AL than AU, suggesting a brief episode of substorm-like activity. Relative auroral quieting with AE ranging between 600 and 200 nT marked the remainder of the day. The interval of concern extends from 1900 to 2400 UT when SYM-H was at or near its most negative values.

[31] Figure 4 shows the responses of auroral boundaries [Newell et al., 1996] to interplanetary fluctuations. Plotted are the magnetic latitudes of B1, B2e, B2i, and B5 observed by five DMSP satellites in the evening and dawn MLT sectors between 1900 and 2130 UT. There are two reasons for the lack of auroral boundaries on the morning side prior to  $\sim 2020$  UT. First, a data gap in DMSP 13 measurements occurred between 1730 and 2000 UT. Second, the other DMSP satellites crossed the auroral oval well onto the dayside and disallow meaningful applications of nightside boundaries [Newell et al., 1996]. Dashed lines on both plots represent least square fits to the magnetic latitudes of the boundaries as functions of UT. They serve only as guides for the eye. The data illustrate that in both the evening and dawn sectors, the magnetic latitudes of B1 and B2e were fairly constant during the period of interest. B5 and B2i systematically shifted toward lower latitudes, indicating that the polar cap expanded and the inner edge of quasi-dipolar field lines moved earthward as the main phase progressed. Near 2020 UT, B2i locations in the evening sector are well equatorward of the trend line at MLat  $< 60^\circ$ , suggesting that the inner magnetotail reconfigured near this time.

#### 4.2. Intense Field-Aligned Currents

[32] Figure 5 shows particle and field data acquired by (a) F15 and (b) F12 in the evening sector and (c) F13 in the

dawn sector, respectively. From top to bottom the panels for each satellite show (1) directional energy flux (E-Flux) in  $\text{eV cm}^{-2} \text{s}^{-1} \text{sr}^{-1}$  of down-coming electrons (upper line) and ions (lower line); (2) directional number fluxes (N-Flux) of down-coming electrons (upper line) and ions (bottom line) with energies between 30 eV and 30 keV, in  $\text{cm}^{-2} \text{s}^{-1} \text{sr}^{-1}$ ; (3) average energy of precipitating ions (upper line) and electrons (lower line), defined as  $E_{\text{AVE}} = E\text{-Flux}/N\text{-Flux}$  (calculated this way,  $E_{\text{AVE}}$  is about twice the mean thermal energy of the species population [Robinson et al., 1987]); (4) the cross-track component of the magnetic field  $\delta B_z$  in nanotesla; and (5) the in-track component of the electric field  $E_y$  calculated from the observed ion drift and IGRF magnetic field values [Rich and Hairston, 1994]. Vertical dashed lines indicate times when the DMSP satellites crossed B1, B2e, B2i, and B5 [Newell et al., 1996]. Data are plotted as functions of UT, MLat, and MLT.

[33] Figure 5a shows that F15 entered the evening sector auroral oval from the southern polar cap (B5) near 2015:30 UT. A rapid rise in electron fluxes (panel 2) and a reversal in  $E_y$  (panel 5) mark the transition. Attention is directed to the  $\sim 1500$  nT decrease in  $\delta B_z$  detected between 2018:10 and 2019:30 UT (panel 4). This nearly uniform decrease in  $\delta B_z$  with time corresponds to a  $2 \mu\text{A/m}^2$  outward FAC or a net electron flux of  $\sim 10^9 \text{ cm}^{-2} \text{s}^{-1}$  into the ionosphere. Figure 5a also shows that down-coming electron fluxes were  $> 10^9 \text{ cm}^{-2} \text{s}^{-1} \text{sr}^{-1}$  in the upward FAC sheet (panel 2). Assuming isotropy over the down-coming hemisphere, we see that electrons with energies between 30 eV and 30 keV can account for the observed upward FAC. The  $E_{\text{AVE}}$  plot (panel 3) indicates that most current-carrying electrons had  $E < 500$  eV. The largest  $\delta B_z$  deflection, marking the interface between upward and downward FAC sheets, occurred near  $-56^\circ$  MLat between the B2i and B2e boundaries. A deflection of 1500 nT corresponds to an integrated FAC  $J_{\parallel}$  of  $\sim 1.2 \text{ A/m}$  or  $\sim 1.2 \text{ MA}$  for every 1000 km extent in longitude ( $\sim 1$  hour in LT). Current continuity requires that a height-integrated Pedersen current  $J_P$ , equal to  $J_{\parallel}$ , flows across the interface between the upward and downward FAC sheets.

[34] Near the transition between the upward and downward FAC sheets, a maximum electric field of  $\sim 40 \text{ mV/m}$  was inferred from drift meter measurements and the local IGRF magnetic field. To facilitate direct comparisons be-

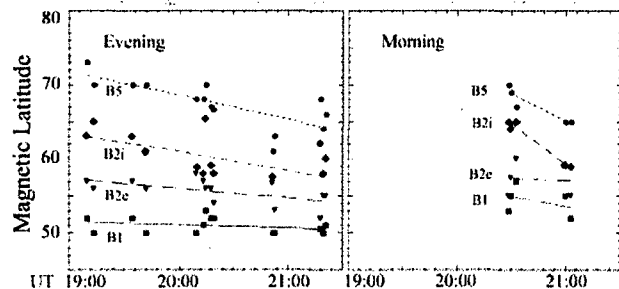


**Figure 4.** Locations of B1, B2e, B2i, and B5 auroral boundaries observed by DMSP satellites in the (left) evening and (right) morning MLT sectors between 1900 and 2200 UT on 6 April 2000.

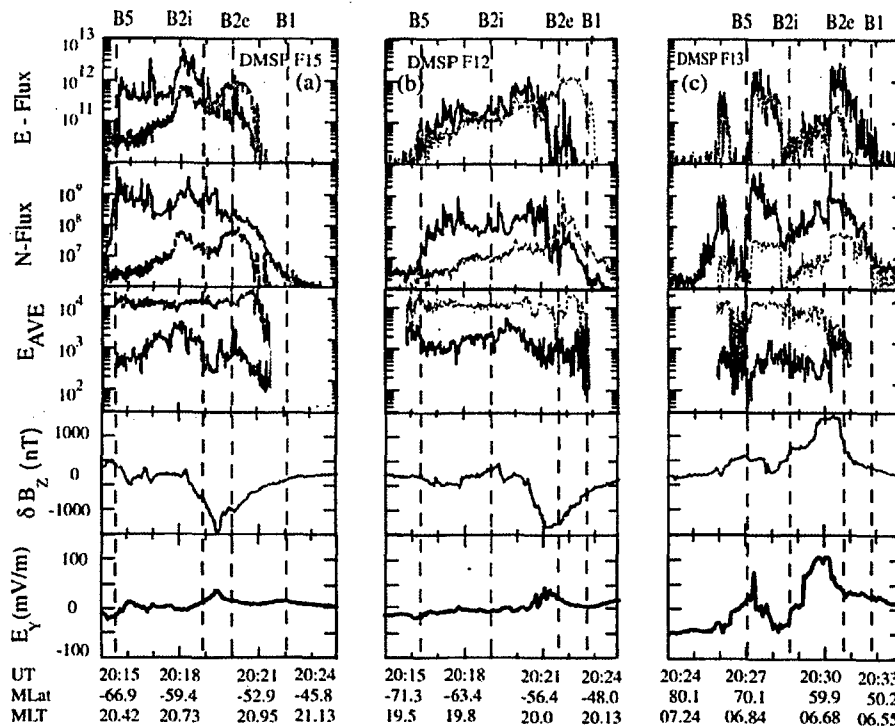


**Figure 5.** Particle and field measurements by (a) DMSP F15 and (b) F12 in the evening sector after 2015 UT, and (c) F13 in the morning sector after 2024 UT on 6 April 2000. From top to bottom the panels for each satellite show: (1) directional energy flux (E-Flux) in  $\text{eV cm}^{-2} \text{s}^{-1} \text{sr}^{-1}$  of down-coming electrons (upper line) and ions (lower line); (2) directional number fluxes (N-Flux) of down-coming electrons (upper line) and ions (bottom line) with energies between 30 eV and 30 keV, in  $\text{cm}^{-2} \text{s}^{-1} \text{sr}^{-1}$ ; (3) average energy of precipitating ions (upper line) and electrons (lower line), defined as  $E_{\text{AVE}} = E\text{-Flux}/N\text{-Flux}$ ; (4) the cross-track component of the magnetic field  $\delta B_z$  in nanotesla; and (5) the in-track component of the electric field  $E_y$  calculated from the observed ion drift and IGRF magnetic field values [Rich and Hairston, 1994]. Vertical dashed lines indicate times when the DMSP satellites crossed B1, B2e, B2i, and B5 [Newell et al., 1996]. Data are plotted as functions of UT, MLat, and MLT. See color version of this figure at back of this issue.

tween electric fields in the evening and dawn MLT sectors, we have plotted  $E_y$  data in panel 5 of Figures 5a, 5b, and 5c on the same scale. This suppresses information, available in standard ion drift meter displays, that indicate a 1 km/s subauroral ionospheric drift event occurred just equatorward of B1 [Anderson et al., 1993]. Magnetic deflections due to R2 currents and subauroral electric fields extend equatorward to approximately  $-45^\circ$  MLat.

[35] Less than 2 min after DMSP F15, F12 crossed the auroral oval near the 20 MLT meridian, where it detected similar  $\delta B_z$  and  $E_y$  variations. Particle fluxes measured by the SSJ4 sensor on F12, shown in Figure 5b panel 2, yield one additional relevant observation that differs significantly from the F15 observations. Data plotted in Figure 5a panels 1 and 2 show that on F15 in the downward FAC region, energy fluxes of down-coming ring current ions exceeded those of precipitating electrons. Electron number fluxes were always greater than ion fluxes. DMSP F12 measurements in Figure 5b panels 1 and 2 indicate that across the downward current sheet (MLat  $> -56^\circ$ ) ion number fluxes were larger than those of electrons by a factor of two or more. The difference is attributed to intense

fluxes of low energy ( $< 1$  keV) ions that the SSJ4 sensor on F12 could detect, but the one on F15 could not.

[36] Figure 6 shows DMSP F12 measurements acquired between 2020 and 2023 UT in greater detail. Figure 6a repeats the  $\delta B_z$  trace. Figure 6b shows the difference between electron and ion number fluxes. The vertical dashed line marks the approximate location of the transition from upward to downward FACs. To the left of this line, where the  $\delta B_z$  trace has a negative slope indicating a current out of the ionosphere, the flux of precipitating electrons exceeds that of the ions by  $\sim 3 \times 10^8/(\text{cm}^2 \text{s} \text{sr})$ . Near 2022 UT the opposite FAC polarity is observed and the precipitating ion flux dominates. Figures 6c and 6d show 5-s averaged electron and ion spectra centered near 2021:00 and 2021:51 UT in the upward and downward FAC sheets, respectively. In the upward FAC sheet, low ( $< 1$  keV) electrons dominate the spectrum. In the downward FAC sheet the flux of  $< 1$  keV ions almost matches that of the electrons. At energies  $> 2$  keV the ion spectrum is relatively flat, indicating the presence of substantial fluxes at energies  $> 30$  keV, the upper limit of SSJ4 detection. As mentioned above, DMSP satellites cannot monitor upward electron or ion fluxes.



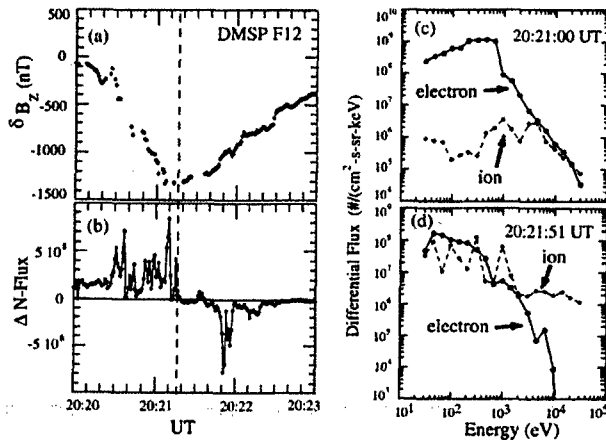


**Figure 6.** Particle and field characteristics of the FAC sheets crossed by DMSP F12 between 2020 and 2023 UT on 6 April 2000. Panels show (a) variations of  $\delta B_z$  and (b) differences between electron and ion number fluxes as a function of UT, as well as 5-s averaged ion and electron spectra measured by SSJ4 within the (c) upward and (d) downward FAC sheets. See color version of this figure at back of this issue.

However, the DMSP F12 observations in Figures 6b and 6d strongly suggest that precipitating ions dominated over precipitating electrons.

[37] Returning to Figure 5c, we see that DMSP F13 data were acquired near the dawn meridian in the northern ionosphere. Electron fluxes (panel 2) rose above polar rain levels at  $\sim 2025:50$  UT. The polarity of  $E_y$  reversed  $\sim 30$  s later. F13 entered the main oval (B5) just before 2027:00 UT. In the region poleward of B5, electron and ion fluxes were often near background levels, leading to large, nongeophysical variations in calculated values of  $E_{AVE}$ . Since the polar cap is outside the domain of concern for this paper, we do not display  $E_{AVE}$  values in this region. A comparison with data in Figure 5a panels 1 and 2 indicates that BPS electron precipitation was more structured in the dawn than in the evening sector [Winningham *et al.*, 1975]. Particle fluxes observed in the morning sector by F11 and F14 (not shown) were similar to those of F13. Electron energy fluxes  $>1 \text{ erg cm}^{-2} \text{ s}^{-1} \text{ sr}^{-1}$  were observed for more than a minute after 2027 and 2030 UT. A pair of intense FAC sheets, with a magnetic deflection  $>1400 \text{ nT}$  ( $\sim 1.1 \text{ A/m}$ ), was observed near 2030 UT (panel 4). A sharp intensification of electron fluxes (panels 1 and 2) marked the transition from downward to upward FAC. In this case,  $E_y \approx 90 \text{ mV/m}$  was inferred from drift meter measurements near the maximum  $\delta B_z$ . In the region of the downward FAC, low ion fluxes indicate that upgoing ionospheric electrons were probably the prime current carriers. Again the maximum deflections in  $E_y$  and  $\delta B_z$  occurred between B2e and B2i. Finally, we note that in both the morning and evening sectors, R2 FACs extended to subauroral latitudes.

[38] An intriguing aspect of the satellite observations concerns  $\delta B_z$  signatures as the FAC system relaxed. Figure 7 shows  $\delta B_z$  signatures observed by (top) F15 and (bottom) F12 during the next evening pass over the northern auroral oval. As the two spacecraft moved poleward into

and across the evening sector of the northern auroral oval, they detected three, rather than two, current sheets, as indicated by the arrows in Figure 7. At low magnetic latitudes both satellites encountered FACs directed out of the ionosphere. Poleward of this upward current sheet they crossed the standard, evening-sector R1/R2 system. No sign of an additional FAC sheet appeared in F13 and F14 measurements as the satellites crossed the southern auroral oval in the morning sector. There are five empirical facts to be noted. (1) The equatorward FACs out of the ionosphere occurred between B1 and B2e. (2) DMSP F15 and F12 measured average upward current densities of  $\sim 1.4 \mu\text{A/m}^2$  and  $1.0 \mu\text{A/m}^2$ , with integrated currents of  $0.56 \text{ A/m}$  and  $0.4 \text{ A/m}$ , respectively. (3) Within the equatorward upward current sheet, electric fields were weak and equatorward. (4) Maximum  $\delta B_z$  deflections at the R1/R2 interface occurred between B2e and B2i. (5) Total  $\delta B_z$  perturbations measured by F15 and F12 in the R2 currents were  $\sim 1400 \text{ nT}$  ( $1.1 \text{ A/m}$ ) and  $1000 \text{ nT}$  ( $0.8 \text{ A/m}$ ), respectively.

[39] Particles monitored by F12 and F15 between B1 and B2e for this pass (not displayed) indicate that electron N-fluxes always exceeded those of ions. In the previous southern hemisphere pass, F12 measurements show that the opposite relationship prevailed (Figure 6). However, ion E-fluxes from the central plasma sheet (between B2e and B2i) were similar to those observed during the southern auroral oval crossing. The discussion section considers implications of these measurements for our understanding of ring current pressure distributions.

[40] Analysis of DMSP data acquired during the magnetic storm was facilitated by the relative spacecraft orbital phasing prevailing on 6 April 2000. F11, F13, and F14 crossed the high-latitude ionosphere in the same hemisphere within 2 min of each other. The F12 and F15 spacecraft flew over the conjugate polar ionosphere  $\sim 10$  min earlier than F11, F13, and F14 but within 1.5 min of each other. Table 1 lists the UT as well as the magnetic and geographic coordinates at which the DMSP satellites crossed the largest FAC perturbations. Value of the largest amplitude of  $|\delta B_z|$

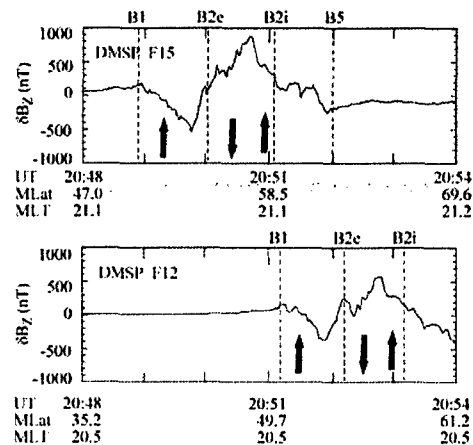


**Figure 7.** Values of  $\delta B_z$  observed by (top) F15 and (bottom) F12 while crossing the northern auroral oval between 2048 and 2054 UT. Upward/downward pointing arrows indicate the polarities of FACs out of/into the ionosphere.



**Table 1.** Extrema of  $\delta B_Z$  and  $E_Y$ 

DMSP	UT	MLAT	MLT	MLONG	GLAT	GLONG	$ \delta B_Z $ , nT	$ E_Y $ , mV/m
F12	2012.2	-56.0°	19.9	66°	-55.0°	14.5°	1326	41.5
F13	2030.3	58.7°	6.7	225°	-63.0°	159.9°	1424	91.5
F14	2030.7	59.0°	8.4	255°	61.2°	199.8°	1354	82.9
F15	2019.4	-55.9°	20.9	79°	-52.1°	26.4°	1506	42.5

appears in the eighth column. Maxima for  $|E_Y|$  were acquired spatially close to, but not necessarily coincident with,  $\delta B_Z$  extrema. Equation (6) indicates that separations in  $|\delta B_Z|$  and  $|E_Y|$  extrema reflect the presence of conductivity gradients near the upward/downward FAC interface.

[41] Three empirical aspects of data in Table 1 call for comment. First,  $\delta B_Z$  extrema measured by all of the satellites corresponded to FACs with  $J_{\parallel} > 1$  A/m. Second, all  $\delta B_Z$  extrema were observed at magnetic latitudes equatorward of 60°. Third, electric fields detected at similar MLTs had comparable values. The latitudinal distributions of  $E_Y$  detected by F11 and F13 were nearly identical across the morning auroral oval. Note, however, that  $E_Y$  values measured in the evening sector were about half those detected on the morning side (compare panel 5 of Figures 5a, 5b, and 5c). Ohm's law dictates that ionospheric conductance was larger in the evening than the morning sector by about a factor of two.

[42] In the remaining analysis of DMSP data we adopt  $|\delta B_Z|_{\max}$  as our organizing parameter for understanding M-I coupling. This choice is dictated by two considerations. First, equation (5) shows that  $|\delta B_Z|_{\max}$  is directly proportional to  $J_{\parallel}$  the integrated FAC coupling the magnetosphere to the ionosphere. As such it maps to the ionospheric footprint of maximum Pedersen current. Second, during the magnetic storm's main phase,  $|\delta B_Z|_{\max}$  was observed at relatively low magnetic latitudes that normally map to the inner magnetosphere, which primarily acts as a current generator [Vasyliunas, 1970]. Figure 8 plots all 57 detections of  $|\delta B_Z|_{\max}$  observed by the four DMSP satellites carrying SSM between 1600 and 2400 UT. For reference, Figure 8 also contains a plot of the AE index. Somewhat arbitrarily we refer to FAC events as intense if  $|\delta B_Z|_{\max} > 1000$  nT. We see that of the 14 intense events, 11 occurred late in the main phase after 2215 UT when AE was generally decreasing after several brief intensifications and SYM-H was either decreasing or oscillating near its minimum value (Figure 3).

[43] Vertical lines on Figure 8 at 2015, 2155, 2250, and 2345 UT highlight intensifications of the FAC system. The events described in Figure 5 and in Table 1 occurred near 2015 UT, shortly after AE decreased by  $\sim 500$  nT (Figure 2). The FAC intensifications appear to occur on fairly rapid time scales. As F13 and F14 crossed the northern auroral oval they detected magnetic perturbations of 646 nT at 2012 UT (MLat = 57.7°, MLT = 18.2) and 797 nT at 2014 UT (MLat = 59.9°, MLT = 20.6), respectively. At 2019 UT, F15 observed a 1506 nT perturbation in the conjugate ionosphere (MLat = -55.9°, MLT = 20.9); 2 min later F12 also crossed the same intense FAC sheet. A similar rapid intensification of FACs occurred shortly after 2200 UT when three satellites measured  $|\delta B_Z|_{\max} \geq 1200$  nT. Note, however, that at  $\sim 2201$  UT, F12 and F15 detected maximum perturbations of 769 and 1317 nT, respectively, while separated by  $< 2^\circ$  in MLat and  $\sim 1$  hour

in MLT. While intensifications of FACs appear four times during the interval plotted in Figure 8, no evidence of sawtooth oscillations appears in particle fluxes observed at geosynchronous orbit [Huang *et al.*, 2003].

### 4.3. Circuit Conductance

[44] The previous section derives relationships between variations of  $\delta B_Z$  and  $E_Y$  required to maintain current continuity in the ionosphere beneath DMSP satellites. Smiddy *et al.* [1980] showed that in regions of nearly uniform conductance equation (6) reduces to  $\Sigma_P = \Delta \delta B_Z / [\mu_0 \Delta E_Y]$ . The symbol  $\Delta$  indicates changes in  $\delta B_Z$  or  $E_Y$ . In practical units  $\Sigma_P$  (mho) =  $\Delta \delta B_Z$  (nT) / [1.256  $\bullet$   $\Delta E_Y$  (mV/m)]. These equations assume that the infinite current sheet approximation is valid. For the events of Figure 5, simultaneous  $\delta B_Z$  and  $\delta B_Y$  variations were nearly monotonic and highly correlated, indicating that the spacecraft indeed crossed quasi-infinite current sheets at nearly constant attack angles  $\alpha = \tan^{-1} (\delta B_Z / \delta B_Y)$ . Values of  $\alpha$  listed in the last column of Table 2 show that the DMSP satellites crossed FAC sheets at nearly normal incidence. Fung and Hoffman [1992] addressed the more general case where end effects or filamentary structures are important.

[45] Table 2 also summarizes information contained in Figure 5. Listed data indicate the beginning UT<sub>1</sub> and duration  $\Delta t$  of intervals in which  $\delta B_Z$  and  $E_Y$  variations were highly correlated, consistent with crossing regions of nearly uniform  $\Sigma_P$ . Correlation coefficients within the current sheets were  $> 0.98$ . Values of  $\Sigma_P$  estimated from  $\delta B_Z$  and  $E_Y$  variations within the intense upward and downward FAC sheets are listed in column 8 of Table 2. Except in the downward FAC sheet crossed by F13, estimated values of  $\Sigma_P$  were  $> 25$  mho.

[46] Measurements from the SSJ4 sensor allow independent estimates of the ionospheric conductance using empirical formulas suggested by Robinson *et al.* [1987].

$$\Sigma_P = [40 E_{ave} \sqrt{(\Phi_E)}] / [16 + E_{ave}^2] \quad (12)$$

and

$$\Sigma_H = 0.45 \Sigma_P (E_{AVE})^{0.85} \quad (13)$$

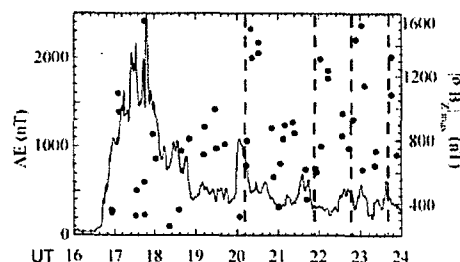


**Figure 8.** Values of AE (solid line) and  $|\delta B_Z|_{\max}$  (circles) plotted as a function of UT.

**Table 2.** Auroral FAC Circuit Parameters

DMSP	UT <sub>i</sub>	$\Delta t$ , s	$\delta B_{Zb}$ , nT	$\delta B_{Zf}$ , nT	$E_{Yb}$ , mV/m	$E_{Yf}$ , mV/m	$\Sigma_p$ , mho	$\alpha$
F13	2028:46	64	600	1340	3.0	105.4	5.9	68.3°
F13	2030:30	21	1370	498	48.5	25.4	30.0	83.9°
F15	2018:22	64	-218	-1487	0.4	37.4	27.3	84.5°
F15	2019:30	76	-1469	-496	34.7	9.8	31.1	89.2°

Here  $E_{AVE}$  represents the average energy of precipitating electrons in keV and  $\Phi_E$  is the electron energy flux in ergs/(cm<sup>2</sup> s). To help estimate ionospheric conductances we assume that electron distribution functions were isotropic over the down-coming hemisphere. Calculated values of  $\Sigma_p$  (top) and  $\Sigma_H$  (bottom) due to energetic electron precipitation observed by F15 (left) and F13 (right) are plotted as functions of UT in Figure 9. The vertical dashed lines mark the intervals during which  $\Sigma_p$  was estimated from highly correlated  $\delta B_Z$  and  $E_Y$  variations. The downward and upward pointing arrows located between the dashed lines signify the directions of FACs into and out of the ionosphere, respectively. Heavy horizontal bars within the dashed lines indicate calculated values of  $\Sigma_p$  listed in Table 2. Comparing Pedersen conductances estimated using two different techniques, we see that the average values of  $\Sigma_p$  estimated from equation (12) were significantly lower than those obtained from equation (7). Attention is directed to the upward current sheets where observed variations of  $\delta B_Z$  and  $E_Y$  were monotonic (Figure 5) and highly correlated. Here equation (6) indicates that  $\Sigma_p$  should have been nearly constant. In both instances  $\Sigma_p$  plots estimated from electron measurements suggest the presence of gradients. We defer comment on these discrepancies to the discussion section.

#### 4.4. Ground Measurements

[47] Black circles on the trajectories of Figure 1 and spacecraft designation in Figure 10 indicate the locations of  $|\delta B_Z|$  and  $|E_Y|$  extrema in magnetic and geographical coordinates. Table 1 lists the exact locations. F12 and F15 were flying over the Indian Ocean to the southeast of the African continent. F13 and F14 were over northeastern Siberia. The  $\delta B_Z$  extrema map to the ionospheric location of the most intense Pedersen currents linking downward and upward FAC sheets. A priori, one might expect that magnetometers at ground stations located beneath these currents would detect comparably large magnetic fluctuations. Cape Schmidt (CPS) at 68.9°N, 180.5°E provides the only magnetic field measurements presently available from the Siberian sector. The station lies about half way between the longitudes of F13 and F14. However, it is  $\sim 6^\circ$  in latitude to the north of these FAC encounters. CPS records show only modest ( $\sim 200$  nT) variations between 2010 and 2100 UT.

[48] The locations of F12 and F15 over the Indian Ocean make direct comparisons with subsatellite magnetometers impossible. No significant magnetic perturbations were recorded at stations arrayed along the coast of Antarctica. Table 1 gives the magnetic latitudes and longitudes of F12 ( $-56^\circ$ ,  $66^\circ$ ) and F15 ( $-55.9^\circ$ ,  $79^\circ$ ). If the inner magnetosphere acts as a current generator [Kan and Sun, 1985], spacecraft flying above the conjugate ionosphere should observe  $\delta B_Z$  signatures similar to those detected by F12 and F15. Consequently, similar magnetic perturbations would

be detected at conjugate ground locations. The magnetic latitude and longitude ( $56.3^\circ$ ,  $74.7^\circ$ ) of the Valentia (VAL) station in Ireland is nearly conjugate to the places where F12 and F13 detected  $\delta B_Z$  extrema. Figure 11 shows the magnitude and three components of magnetic perturbations observed at VAL between 1400 and 2100 UT. Variations measured between 2000 and 2100 UT were  $< 100$  nT. An examination of records from a large number of auroral and middle latitude stations shows that magnetic variations commensurate with those observed by DMSP were not detected on the ground. Interested readers may verify this conclusion by examining the many ground magnetic records for 6 April 2000, available on the Kyoto web site (<http://swdcd.db.kugi.kyoto-u.ac.jp/index.html>).

#### 5. Discussion

[49] The previous section shows particle and field measurements acquired during the main phase of the 6 April 2000 magnetic storm, focusing on nearly simultaneous observations of intense ( $J_{||} > 1$  A/m) FACs in the evening and dawn MLT sectors. Large magnetic perturbations, marking the R1/R2 transition, occurred between the B2e and B2i auroral boundaries [Newell et al., 1996]. Height-integrated conductivities estimated from electric and magnetic field variations [Smiddy et al., 1980] were systematically larger than those determined from electron fluxes [Robinson et al., 1987]. Larger electric fields appeared in the morning than in the evening sector, with similar FAC inputs. Finally, available data from ground stations show no commensurate magnetic perturbations while DMSP was detecting intense FACs.

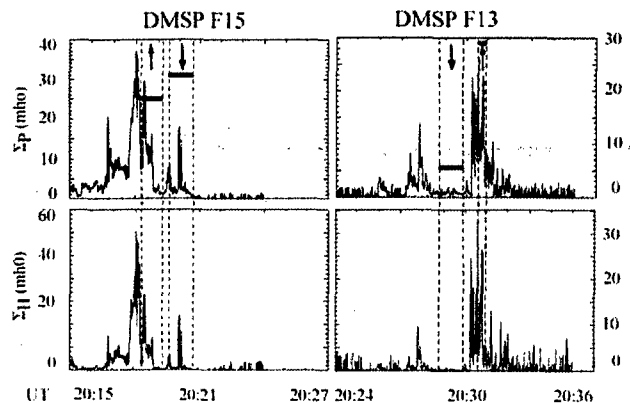


**Figure 9.** (Top) values of  $\Sigma_p$  and (bottom)  $\Sigma_H$  estimated from energetic electron fluxes measured by (left) F15 and (right) F13 plotted as functions of UT. The heavy horizontal lines indicate values of  $\Sigma_p$  estimated from  $\delta B_Z$  and  $E_Y$  variations.

### Distribution of Geomagnetic Observatories

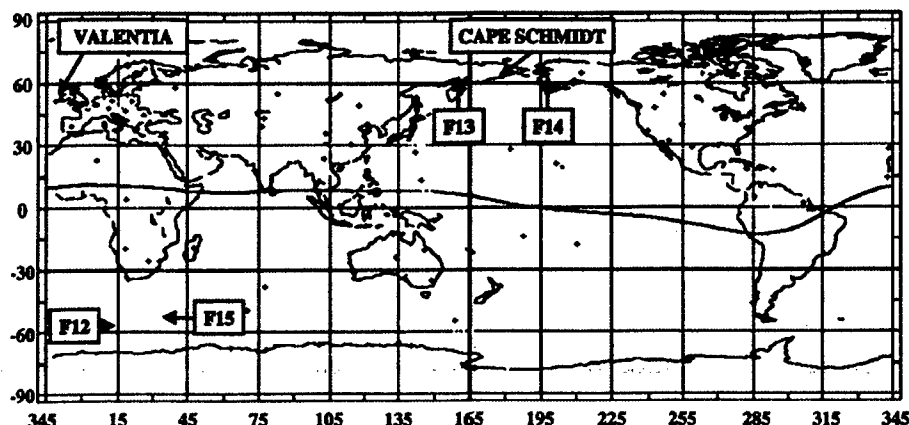


**Figure 10.** World map showing the positions of four DMSP satellites when they encountered extrema of  $|\delta B_z|$  and  $|E_y|$ . Locations of the Cape Schmidt (CPS), Memambetsu (MEM), and Valentia (VAL) magnetic stations are indicated for reference.

[50] Observations presented here are unusual but not unique. An informal survey of DMSP measurements revealed that  $J_{\parallel} > 1$  A/m events regularly occur during the main phases of magnetic storms with  $Dst < -200$  nT. Distinct ground signatures accompanied many, but not all, of the intense stormtime FAC events. At the suggestion of G. Lu (private communication, 2002), we examined DMSP particle and field data acquired during the superstorms of 15 July 2000 and 31 March 2001. DMSP measurements during both storms bore striking similarities to the observations reported here. Again intense FACs observed at 840 km were unmatched by strong magnetic perturbations at the ground. In both of these superstorms the intense FACs were observed at latitudes well equatorward of the normal auroral oval, and  $E_{AVE} \leq 500$  eV for precipitating electrons.

[51] This section discusses (1) some implications of DMSP observations for understanding the dynamics of magnetospheric plasma pressure distributions, (2) applications of Ohm's law in the ionosphere, (3) the absence of FAC magnetic signatures on the ground, and (4) current carriers.

#### 5.1. Magnetospheric Pressure Distributions

[52] The intense FACs crossed by DMSP satellites in the evening and dawn MLT sectors developed during the storm's main phase. Activity detected at the latitudes of auroral electrojet stations was generally quieting but was also subject to sporadic increase/decrease cycles (Figures 3 and 8). The negative slope of the SYM-H index during the period of interest indicates that the ring current intensified and/or moved closer to Earth. The fact that the latitude of B1 was stable and that  $\delta B_z$  and  $E_y$  were confined to MLat  $> 45^\circ$  suggests that the ring current's inner edge did not move much further earthward. Moving the ring current earthward of  $L = 2$  requires that a significant dawn-dusk electric field penetrate more closely to Earth. This inference is consistent with CRRES observations that ring current ions did not move to  $L < 2$  during the magnetic storms of June and July 1991 [Burke et al., 1998; Wilson et al., 2001].

[53] Vasyliunas [1970] showed that field-aligned currents  $j_{\parallel}$  flow into or out of the ionosphere whenever gradients of the magnetospheric plasma pressure  $p$  are not aligned with gradients in magnetic flux tube volumes  $\xi = \int (ds/B)$

$$j_{\parallel} = -(B_m/(2B_e)b_e \cdot [\nabla_p \times \nabla \int (ds/B)]), \quad (14)$$

where  $b_e$  is a unit vector along the Earth's magnetic field at the equator ( $B_e$ ) and  $B_m$  is the magnetic field at the top of the ionosphere.  $\nabla \xi$  has a strong radially outward component at all local times. Magnetospheric pressure distributions estimated by Wing and Newell [1998] from ion fluxes observed between B2i and B5 indicate that pressure maxima occur in the midnight to late evening MLT sector at distances from the Earth that depend on the level of geomagnetic activity. In the inner magnetosphere near the

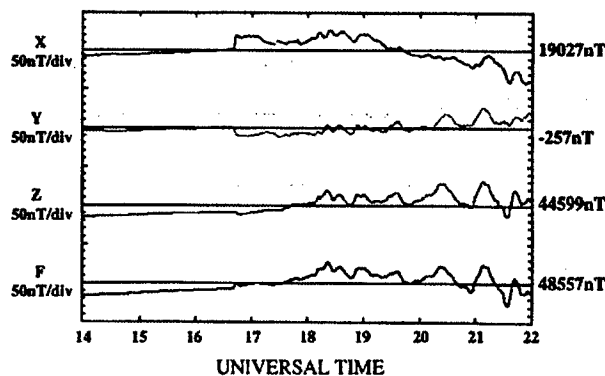


**Figure 11.** Three components and intensity of magnetic perturbations measured at Valentia between 1400 and 2100 UT on 6 April 2000. Numbers listed to the right of the plots indicate baseline values from which perturbations are measured.

dusk (dawn) meridians where  $\nabla\xi$  is mostly radial, we expect FACs into (out of) the ionosphere in the evening (morning) sector due to the eastward (westward) pressure gradients.

[54] Beyond the B2i boundary, azimuthal pressure gradients appear weak [Wing and Newell, 1998] but still maintain maxima close to the midnight meridian. The location of the largest  $\delta B_z$  and  $E_y$  perturbations between B2e and B2i indicates that the transition between R2 and R1 currents occurred in the inner part of the central plasma sheet. This conclusion agrees with the work of Wing and Newell [2000] who show that R1 FACs are generated tailward of B2i under quiet conditions and that the transition between R1 and R2 occurs between B2i and B2e.

[55] The concept of magnetospheric plasma pressure gradients controlling the distribution of ionospheric FAC distributions [Vasyliunas, 1970] provides guidance for understanding the FAC sheet out of the ionosphere observed by F12 and F15 at low ( $\sim 50^\circ$ ) magnetic latitudes near 2050 UT. Comparisons of  $\delta B_z$  measurements in the southern and northern hemispheres (Figures 5 and 7) show that while B2i and B5 moved equatorward by  $\sim 2^\circ$ , the magnetic latitudes of B1 and B2e were steady. The  $\sim 650$  nT decrease in  $\delta B_z$  seen by F15 between 2049:00 and 2049:50 UT indicates that a FAC of  $\sim 1.6 \mu\text{A}/\text{m}^2$  flowed out of the ionosphere. The average intensity of the downward FAC encountered between 2049:50 and 2050:50 UT was  $\sim 3 \mu\text{A}/\text{m}^2$ , about twice its southern hemisphere value. The outward FAC observed by F12 and F15 between B1 and B2e requires that close to the inner edge of the plasma sheet near 2100 MLT,  $\nabla p$  had a westward component. In the central plasma sheet, between the mappings of B2e and B2i, the eastward component of  $\nabla p$  intensified.

[56] The requirement for a westward pressure gradient in the innermost plasma sheet suggests the following scenario. The brief burst of substorm-like activity observed near 2000 UT (cf. AE trace in Figure 7) injected plasma close to the Earth in the midnight sector. Because of the short time allowed for the injection and ring current shielding of magnetospheric electric fields, the pressure maximum was between the mapping of B2e and B2i. However, a large number of energetic ions reached the mapped location of B1. When the substorm driver suddenly turned off, gradient-curvature drifts dominated ion motion. Most of the pressure was carried by westward drifting energetic ions. The gradient drift velocity  $V_G$  of an energetic ion is

$$V_G = (\mu_i/qB^2)\mathbf{B} \times \nabla B, \quad (15)$$

where  $\mu_i$  the ion's magnetic moment is a constant of the motion. In a magnetic dipole approximation  $B$  is proportional to  $R^{-3}$ , where  $R$  is the distance from the center of the Earth. Thus  $V_G$  is proportional to  $R^{-1}$ . Since  $V_G = R d\phi/dt$ , the rate at which energetic ions drift in local time to the west is proportional to  $R^{-2}$ . Although we lack information about the magnetic field structure in the equatorial plane, our approximation suggests that the earthward part of the injected plasma drifts to the west at a much faster angular speed than the part initially further from the Earth in the main plasma sheet (poleward of B2e).

[57] If dynamics observed during the magnetic storm of June 1991 were repeated on 6 April 2000, then inflationary

effects of the ring current should have caused the equatorial mapping of B1 to lie closer to 6 than to 3  $R_E$  from the center of the Earth [Burke et al., 1998]. Under these circumstances,  $\nabla B$  should have been unusually strong between the mappings of B1 and B2e. Assuming that the part of the ring current population B1 and B2e covered a relatively narrow swath in local time, it appears plausible that the centroid of plasma pressure gradient-curvature drifted to the west of the DMSP F12 and F15 orbits. In the evening sector  $\nabla p$  would have had a westward component to drive an outward FAC. From the perspective of current-carrying particles, between B1 and B2e SSJ4 detected larger (smaller) fluxes of precipitating electrons than down-coming ions in the northern (southern) hemisphere pass.

## 5.2. Ionospheric Ohm's Law

[58] Plots in Figure 9 compare values of  $\Sigma_p$  calculated using electron fluxes measured by the SSJ4 sensors on DMSP F15 and F13 [Robinson et al., 1987] with estimates based on simultaneous electric and magnetic field variations observed with SSIES and SSM [Smiddy et al., 1980]. Except in the region of upward FACs detected by F13, values of  $\Sigma_p$  estimated using the electromagnetic technique are much higher. We suggest three reasons for this discrepancy. First, electromagnetic calculations of  $\Sigma_p$  are most valid along trajectory segments where the conductance is nearly constant. Distributions of  $\Sigma_p$  determined from electron fluxes suggest that this condition was not always met. Second, during the main phase of this storm M-I coupling conditions exceeded the limits of validity for applying the formulas of Robinson et al. [1987]. Third, the equation derived by Smiddy and coworkers assumes that the M-I circuit has reached a steady state. F13 and F14 detected relatively small values of  $|\delta B_z|_{\text{max}}$  in the evening auroral oval a few minutes before F12 and F15 (Figure 8). These observations suggest that F15 data presented in Figure 5a were acquired soon after the intense FAC circuit was activated. It takes several Alfvén bounce periods for the M-I circuit to reach equilibrium [Kan and Sun, 1985]; thus we must also consider transmission line effects. We address these possibilities in turn.

### 5.2.1. Conductance Gradients

[59] A cursory look at variations in energetic electron fluxes measured by DMSP satellites while crossing individual FAC sheets shows that  $\Sigma_p$  gradients must exist on small spatial scale sizes. Indeed, small-scale variations in  $\delta B_z$  and  $E_y$  traces attest to the presence of similar-scale  $\Sigma_p$  gradients. For two reasons we believe that conductance gradients are not as severe as suggested by estimates presented in Figure 9. First, in choosing regions to estimate  $\Sigma_p$  from  $\delta B_z$  and  $E_y$  variations, we required that the correlation between the two data sets exceed 0.98. Second, in the vicinity of  $\delta B_z$  and  $E_y$  extrema, conductances calculated using the formulas of Robinson et al. [1987] are inconsistent with simple applications of Ohm's law. At  $\delta B_z$  extrema  $J_{\parallel} = I_p = \Sigma_p E_y$ , independent of conductivity profiles. Here  $\Sigma_p$  represents the local value of the Pedersen conductance at the transition between upward and downward FACs. In these regions the formulas of Robinson et al. [1987] predict  $\Sigma_p$  values of a few mhos. For the cases shown in Figures 5a and 5c,  $J_{\parallel} \approx 1.2$  A/m. F13 and F15 measured  $E_y$  values of 91.5 and 42.5 mV/m (Table 1), respectively. Corresponding  $\Sigma_p$  values

**Table 3.** Alfvén Wave Reflection Coefficients

DMSP/j <sub>  </sub>	$\Delta\delta B_Z/\Delta E_Y$	$\Sigma_P/\Sigma_A$	R	$E_Y$ , mV/m	$\delta B_Z$ , nT
F13 $\uparrow$	$7.40 \times 10^{-6}$	5.5	-0.70	338	435
F13 $\downarrow$	$3.79 \times 10^{-5}$	28.4	-0.93	329	452
F15 $\uparrow$	$3.43 \times 10^{-5}$	18.9	-0.90	369	668
F15 $\downarrow$	$3.91 \times 10^{-5}$	21.5	-0.91	277	509

of 13.1 and 28.2 mho exceed those shown in Figure 9 between the upward and downward current sheets. Thus,  $\Sigma_P$  gradients alone cannot account for the difference between the two methods of estimation.

### 5.2.2. Applicability Limits of Robinson Formulas

[60] At large solar zenith angles Robinson's formulas estimate  $\Sigma_P$  and  $\Sigma_H$  for a given energy flux and average energy of precipitating electrons. Robinson *et al.* [1987] excluded contributions to conductances of precipitating electrons with energies <500 eV and all protons and cautions against use of this formula when electron energies are low. During the April 2000 magnetic storm, neglect of these conditions leads to serious underestimates of  $\Sigma_P$ . Data in Figure 5 indicate that the average electron energy was below 500 eV. These electrons are stopped through collisions with thermospheric neutrals at altitudes above 190 km [Rees, 1964]. Ionization created by these incident electrons places the Pedersen current-closure layer at *F* layer altitudes. Few electrons had sufficient energy to create *E*-region ionization (Figure 6c). Recall, too, that in the evening sector, precipitating ions carried the downward FAC (Figure 6d). Galand and Richmond [2001] and Galand *et al.* [2001] showed that precipitating protons significantly affect ionospheric conductance. Determining quantitative relationships between  $\Sigma_P$  and precipitating ions/electron fluxes is beyond the scope of this report.

[61] Uncritical applications of the Robinson formulas, irrespective of location on the globe, can also lead to significant errors. Assume that at  $\delta B_Z$  extrema, the SSJ4 sensors on F13 and F15 measured the same values of  $\Phi_E$  and  $E_{AVE}$ . The Robinson formulas predict the same values of  $\Sigma_P$  and  $\Sigma_H$  beneath the two satellites. This cannot be correct. Pedersen conductivity is given by  $\sigma_P \approx (ne/B) \bullet (v_{in}/\omega_i)$ , where  $n$ ,  $v_{in}$ , and  $\omega_i$  represent the plasma density, the ion-neutral collision frequency, and the ion gyrofrequency, respectively. To a first approximation, electrons precipitating at the locations of F13 and F15 would produce the same plasma density profiles. Assuming similar thermospheric profiles, the  $v_{in}$  height profiles should also be similar. However, since  $\sigma_P$  is proportional to  $B^{-2}$  in the Pedersen current layer, values of  $\Sigma_P = \int \sigma_P ds$  should be quite different. The magnetic field measured by F13 was 1.58 times that observed by F15. Thus for the same particle inputs,  $\Sigma_P$  at the location of F13 would be  $\sim 40\%$  of that at the location of F15. At the interface between the two FACs, we estimated that at the location of F13  $\Sigma_P$  was 46% of the value at F15. On this empirical basis, we join Kamide *et al.* [1981] and Raeder *et al.* [2001] in cautioning that integration of space measurements into AMIE simulations of superstorms must be exercised with great care lest they produce misleading results.

### 5.2.3. Transmission Line Effects

[62] From an electrodynamic point of view, obliquely propagating Alfvén waves carry the FACs [Kan and Sun,

1985]. Quasi-steady state currents represent standing wave structures resulting from the superposition of incident (i) and reflected (r) waves. Electric and magnetic field sensors on polar-orbiting satellites detect superposed perturbation fields. In the infinite current sheet approximation, the fields are  $E_Y = E_Y^i + E_Y^r$ , and  $\delta B_Z = \delta B_Z^i + \delta B_Z^r$ . The incident and reflected electric fields are related through the relationship  $E_Y^r = R E_Y^i$ , where the reflection coefficient  $R = (\Sigma_A - \Sigma_P)/(\Sigma_A + \Sigma_P)$ . The term  $\Sigma_A = 1/(\mu_0 V_{AR})$  is called the Alfvén conductance;  $V_{AR}$  is the Alfvén speed in the reflection layer. Observed above the reflection layer, the incident and reflected waves are seen as propagating at the local Alfvén speed  $\pm V_{AS}$ , i.e.,  $E_Y^i/\delta B_Z^i = V_{AS} = -E_Y^r/\delta B_Z^r$ . Thus  $\delta B_Z^r = -R \delta B_Z^i$ .

[63] The ratio of magnetic to electric field variations at the satellite altitude is given by

$$\left[ \frac{\delta B_Z}{E_Y} \right]_{\text{measured}} = \frac{\delta B_Z^i + \delta B_Z^r}{E_Y^i + E_Y^r} = \frac{1}{(V_{AS})} \frac{1-R}{1+R} = \frac{1}{(V_{AS})} \frac{\Sigma_P}{\Sigma_{AR}}. \quad (16)$$

The IGRF model provides estimates of *B* at any altitude in the ionosphere. Local plasma densities are measured by SSIES. Across regions of interest, O<sup>+</sup> ions were the dominant species. With this information, we can calculate local values of the Alfvén speed,  $V_{AS}$ . Knowing  $V_{AR}$  requires unavailable information about the density and mean mass of ions in the reflection layer. However, equation (16) allows us to use measured values of  $V_{AS}$ ,  $\delta B_Z$ , and  $E_Y$  to calculate the ratio  $\Sigma_P/\Sigma_{AR}$  and determine the reflection coefficients *R*.

[64] Table 3 combines  $\delta B_Z$  and  $E_Y$  observed by F13 and F15 in upward and downward FAC sheets (Table 2) with measured values of  $V_{AS}$  to calculate  $\Sigma_P/\Sigma_A$  and *R*. Columns 5 and 6 of Table 3 show the calculated intensities of electric and magnetic fields for incident Alfvén waves  $E_Y^i = E_Y/(1+R)$  and  $\delta B_Z^i = \delta B_Z/(1-R)$ . Except for the downward FAC crossed by F13, reflection coefficients are near 0.9. In all cases the  $E_Y$  values are much larger than are typically observed at 840 km. Note, however, that in all cases the ratio  $\Delta E_Y/\Delta \delta B_Z$  agrees with the local Alfvén speed derived from plasma densities and total magnetic field measurements. Poynting fluxes carried by the incident waves are of order  $0.1 \text{ W/m}^2 = 100 \text{ erg/(cm}^2 \text{ s)}$ . Although 50 to 80% of this energy is reflected, the Joule heat absorbed by the ionosphere and thermosphere greatly exceeds the energy deposited by precipitating electrons and ions.

[65] Our analysis of DMSP electric and magnetic field measurements provides information about the ratio  $\Sigma_P/\Sigma_A$  but nothing about the value of either quantity. Data presented in the third column of Table 3 indicate that  $\Sigma_P/\Sigma_A$  ratios are relatively large. At ionospheric altitudes Alfvén impedances are typically of the order of 1 mho. Thus  $\Sigma_P$  values are easy to reconcile with estimates in Table 2. On the other hand, if we assume that  $\Sigma_P$  has values determined using the formulas of Robinson *et al.* [1987], then proportionately lower values of  $\Sigma_{AR}$  are required. This in turn requires that  $V_{AR} > V_{AS}$ , a conclusion that is difficult to reconcile with plasma density profiles that typically decrease exponentially with altitude in the topside ionosphere.

[66] The fact that SSIES and SSM detect superposed downward and upward propagating Alfvén waves has practical consequences. Measurements of  $\delta B_Z$  and  $E_Y$  can

be used to estimate the Poynting fluxes associated with the current-carrying waves. Equation (10) indicates that the net Poynting flux is a direct measure of Joule heat dissipated in the ionosphere magnetically conjugate to the spacecraft. Attention is redirected to the large FAC structure centered near 2031 UT in panel 4 of Figure 5c. We have calculated Poynting fluxes between  $55.5^\circ$  and  $61.7^\circ$  MLat. The maximum net Poynting flux was  $\sim 0.11$  W/m<sup>2</sup>. The integrated electromagnetic energy flowing into the ionosphere across the structure was  $\sim 4.2 \times 10^4$  W/m (cf. equation (11)). Measurements from multiple DMSP satellites indicate that the large FAC structures extend for at least an hour in local time. Over a  $15^\circ$  spread in longitude the total power input to the ionosphere exceeds 0.04 TW. DMSP data also indicate that the lifetime of these structures is  $\sim 20$  min.

[67] If we assume that the FAC systems detected by DMSP satellites occurred in both hemispheres and extended for 3 hours in local time in both the evening and morning sectors, their total Joule heat input to the ionosphere in 20 min would be  $\sim 144$  TJ. This represents  $\sim 4\%$  of the total kinetic energy of the ring current particles estimated using the Dessler-Parker-Sckopke relation with  $Dst = -250$  nT [Carovillano and Maguire, 1968]. We suggest that FACs can act as significant coolants for ring current populations and, along with intense fluxes of precipitating ions [Borovsky *et al.*, 1998], partly explain differences between predicted and observed ring-current ion spectra during the June 1991 magnetic storm [Garner *et al.*, 2004].

[68] Finally, our analyses relating FACs to Alfvén waves and to magnetospheric pressure gradients are not necessarily self-consistent. The Vasyliunas/RCM model describes quasi-steady state developments of magnetospheric electrodynamics that are averaged over several Alfvén bounce periods. Song and Lysak [2000] have pointed out that current-carrying Alfvén waves can be generated via the mode conversion of compressive magnetohydrodynamic (MHD) waves. Analyzing the possible role of MHD mode conversion is well beyond the scope of this observational report. However, we note that the compressive modes are intimately tied to variations of magnetic field intensities and plasma pressures. Our superstorm data suggest that the growth and decay of large FAC structures in the ionosphere reflect the dynamics of magnetospheric plasma pressure distributions. Uncovering the physical details of mechanisms responsible for large amplitude, ultra low frequency Alfvén waves associated with FACs represents a fruitful avenue in space research to expand understanding of M-I coupling.

### 5.3. Absence of Ground Magnetic Responses

[69] In absolute terms ground magnetometers continued to observe significant perturbations during the interval after 2000 UT. SYM-H and AE indices were near  $-200$  and  $500$  nT, respectively (Figure 2). Ring current effects are clearly visible in magnetic records from stations at low to middle magnetic latitudes. Relatively high levels of activity persisted at the latitudes of auroral electrojet stations, well poleward of the transient but intense FAC sheets reported here. At first glance the fact that FACs associated with  $|\delta B_z| > 1200$  nT produce ground magnetic perturbations  $< 100$  nT appears surprising. We note, however, that near the extrema of  $\delta B_z$  and  $E_y$  values of  $\Sigma_H$  estimated from fluxes of precipitating electrons are very low (Figure 9).

Fukushima [1976] predicted that FACs, closed only by Pedersen currents, produce no magnetic perturbations at the ground. Perturbations detected on the ground mostly come from Hall currents. With low values of  $\Sigma_H$ , Hall currents are weak. We contend that the combined DMSP and ground measurements constitute an empirical validation of Fukushima's prediction.

### 5.4. Precipitation Fluxes

[70] As mentioned above, the dominant species observed by DMSP F12 in the interval from 2021:15 to 2022:30 UT appear to be precipitating ions. This can be seen from the number flux plot in the panel 2 of Figure 5b. Figure 6 explicitly shows the difference between electron and ion number fluxes. In the upward FAC region, there is a net flux of precipitating electrons. However, in the downward FAC region the precipitating ion flux dominates. Ion and electron spectra on the right side of Figure 6 illustrate the difference in the particle populations with access to the ionosphere in the bipolar current sheets.

[71] The SSJ4 measurements raise fundamental questions for modelers: What dynamics are responsible for episodes in which normally trapped ions, over a broad range of energies, are suddenly dumped into the ionosphere? Examining ion spectra at magnetic latitudes between B2e and B2i measured by F12 and F14 before and after the FAC event shown in Figure 6 leads us to believe that the ion deposition of Figure 6d represents a temporal effect. A broad spectrum of ions that were previously trapped on flux tubes mapping to MLat  $\approx 55^\circ$  precipitate. The energy range of affected ions seems to rule out pitch-angle scattering via gyroresonant wave-particle interactions [Kennel and Petschek, 1966]. In the magnetosphere trapped ions follow guiding-center trajectories along which the first ( $mv_\perp^2/B$ ) and second ( $\int m v_\parallel ds$ ) adiabatic invariants are constants of the motion. If the length of affected magnetic flux tubes decreases during intervals significantly longer than an ion bounce period, in conserving the second invariant a particle's  $v_\parallel$  increases and its pitch angle decreases. This lowers mirror altitudes, allowing some previously trapped ions to become lost in the ionosphere. Why would such a field-line shortening occur? One possible source is a compression of the magnetic field due to an injection of plasma from the magnetotail. This is not the place to answer these questions raised by the DMSP measurements. However, from either quasi steady-state [Vasyliunas, 1970] or dynamical [Song and Lysak, 2000] points of view, the answers involve interactions between plasma-pressure and magnetic-field distributions in the highly stressed inner magnetosphere that are still not understood.

[72] **Acknowledgments.** Research presented in this report was supported in part by Air Force Research Laboratory contract F19628-C-02-0012 with Boston College and by Air Force Office of Scientific Research Task 2311SDA3. The authors are especially grateful to L. C. Gentile for editorial assistance with the manuscript and to F. J. Rich of AFRL and E. Mishin of Boston College for their generosity in making DMSP data available to us in convenient forms.

[73] Arthur Richmond thanks Trevor Garner and another reviewer for their assistance in evaluating this paper.

### References

- Anderson, P. C., W. B. Hanson, R. A. Heelis, J. D. Craven, D. N. Baker, and L. A. Frank (1993), A proposed production model of rapid

- subauroral ion drifts and their relationship to substorm evolution, *J. Geophys. Res.*, **98**, 6069.
- Borovsky, J. E., M. F. Thomsen, R. C. Elphic, T. E. Cayton, and D. J. McComas (1998), The transport of plasma sheet material from the distant tail to geosynchronous orbit, *J. Geophys. Res.*, **103**, 20,297.
- Burke, W. J., J. S. Machuzak, N. C. Maynard, E. M. Basinska, G. M. Erickson, R. A. Hoffman, J. A. Slavin, and W. B. Hanson (1994), Auroral ionospheric signatures of the plasma sheet boundary layer in the evening sector, *J. Geophys. Res.*, **99**, 2489.
- Burke, W. J., N. C. Maynard, M. P. Hagan, R. A. Wolf, G. R. Wilson, L. C. Gentile, M. S. Gussenhoven, C. Y. Huang, T. W. Garner, and F. J. Rich (1998), Electrodynamics of the inner magnetosphere observed in the dusk sector by CRRES and DMSP during the magnetic storm of June 4–6, 1991, *J. Geophys. Res.*, **103**, 29,399.
- Carovillano, R. L., and J. J. Maguire (1968), Magnetic energy relationships in the magnetosphere, in *Physics of the Magnetosphere*, edited by R. L. Carovillano, J. F. McClay, and H. R. Radoski, p. 290, D. Reidel, Norwell, Mass.
- DeCoster, R. J., and L. A. Frank (1979), Observations pertaining to the dynamics of the plasma sheet, *J. Geophys. Res.*, **84**, 5099.
- Dessler, A. J. (1984), The evolution of arguments regarding the existence of field-aligned currents, in *Magnetospheric Currents*, *Geophys. Monogr. Ser.*, vol. 28, edited by T. A. Potemra, p. 22, AGU, Washington D. C.
- Egeland, A. (1984), Kristin Birkeland: The man and the scientist, in *Magnetospheric Currents*, *Geophys. Monogr. Ser.*, vol. 28, edited by T. A. Potemra, p. 1, AGU, Washington D.C.
- Erickson, G. M., and R. A. Wolf (1980), Is steady state convection possible in the earth's magnetosphere?, *Geophys. Res. Lett.*, **6**, 897.
- Fukushima, N. (1976), Generalized theorem for no ground magnetic effect of vertical currents connected with Pedersen currents in the uniform conducting ionosphere, *Rep. Ionos. Space Res. Jpn.*, **30**, 35.
- Fung, S. F., and R. A. Hoffman (1992), Finite geometry effects of field-aligned currents, *J. Geophys. Res.*, **97**, 8569.
- Galand, M., and A. D. Richmond (2001), Ionospheric electrical conductances produced by auroral proton precipitation, *J. Geophys. Res.*, **106**, 117.
- Galand, M., T. J. Fuller-Rowell, and M. V. Codrescu (2001), Response of the upper atmosphere to auroral protons, *J. Geophys. Res.*, **106**, 127.
- Galperin, Y. I., and Y. I. Feldstein (1991), Auroral luminosity and its relation to magnetospheric plasma domains, in *Auroral Physics*, edited by C.-I. Meng, M. J. Rycroft, and L. A. Frank, p. 207, Cambridge Univ. Press, New York.
- Garner, T. W., R. A. Wolf, R. W. Spiro, W. J. Burke, B. G. Fejer, S. Sazykin, J. L. Roederer, and M. R. Hairston (2004), Magnetospheric electric fields and plasma sheet injection to low-L shells during the 4–5 June 1991 magnetic storm: Comparison between the Rice Convection Model and observations, *J. Geophys. Res.*, **109**, A02214, doi:10.1029/2003JA010208.
- Gussenhoven, M. A., D. A. Hardy, and N. Heinemann (1983), Systematics of the equatorward diffuse auroral boundary, *J. Geophys. Res.*, **88**, 5692.
- Hardy, D. A., L. K. Schmidt, M. S. Gussenhoven, F. J. Marshall, H. C. Yeh, T. L. Shumaker, A. Huber, and J. Pantazis (1984), Precipitating electron and ion detectors (SSJ/4) for block 5D/Flights 4–10 DMSP satellites: Calibration and data presentation, *Tech. Rep. AFGL-TR-84-0317*, Air Force Geophys. Lab., Hanscom Air Force Base, Mass.
- Harel, M., R. A. Wolf, P. H. Reiff, R. W. Spiro, W. J. Burke, F. J. Rich, and M. Smiddy (1981), Quantitative simulation of a magnetospheric substorm: I. Logic and overview, *J. Geophys. Res.*, **86**, 2217.
- Huang, C. S., G. D. Reeves, J. E. Borovsky, R. M. Skoug, Z. Y. Pu, and G. Le (2003), Periodic magnetospheric substorms and their variation with solar wind parameters, *J. Geophys. Res.*, **108**(A6), 1255, doi:10.1029/2002JA009704.
- Iijima, T., and T. A. Potemra (1976), Field-aligned currents in the dayside cusp observed by TRIAD, *J. Geophys. Res.*, **81**, 5971.
- Iijima, T., and T. A. Potemra (1978), Large scale characteristics of field-aligned currents associated with substorms, *J. Geophys. Res.*, **83**, 599.
- Kamide, Y., A. D. Richmond, and S. Matsushita (1981), Estimation of ionospheric electric fields, ionospheric currents, and field-aligned currents from ground magnetic records, *J. Geophys. Res.*, **86**, 801.
- Kan, J. R., and W. Sun (1985), Simulation of the westward traveling surge and Pi2 pulsations during substorms, *J. Geophys. Res.*, **90**, 10,911.
- Kennel, C. F., and H. E. Petschek (1966), Limit on stably trapped particle fluxes, *J. Geophys. Res.*, **71**, 1.
- Kivelson, M. G., and H. E. Spence (1988), On the possibility of quasi-static convection in the quiet magnetotail, *Geophys. Res. Lett.*, **13**, 1541.
- Newell, P. T., Y. I. Feldstein, Y. I. Galperin, and C.-I. Meng (1996), Morphology of nightside precipitation, *J. Geophys. Res.*, **101**, 10,737.
- Raeder, J., R. L. McPherron, L. A. Frank, S. Kokubun, G. Lu, T. Mukai, W. R. Peterson, J. B. Sigwarth, H. J. Singer, and J. A. Slavin (2001), Global simulation of the geospace environment modeling substorm challenge event, *J. Geophys. Res.*, **106**, 381.
- Rees, M. H. (1964), Note on the penetration of electrons into the Earth's atmosphere, *Planet. Space Sci.*, **12**, 722.
- Rich, F. J., and M. Hairston (1994), Large-scale convection patterns observed by DMSP, *J. Geophys. Res.*, **99**, 3827.
- Richmond, A. D. (1992), Assimilative mapping of ionospheric electrodynamics, *Adv. Space Res.*, **6**(1), 59.
- Richmond, A. D., and Y. Kamide (1988), Mapping electrodynamic features of the high-latitude ionosphere from localized observations: Technique, *J. Geophys. Res.*, **93**, 5741.
- Robinson, R. M., R. R. Vondrak, K. Miller, T. Dabbs, and D. Hardy (1987), On calculating ionospheric conductances from the flux and energy of precipitating electrons, *J. Geophys. Res.*, **92**, 2565.
- Smiddy, M., W. J. Burke, M. C. Kelley, N. A. Saffelos, M. S. Gussenhoven, D. A. Hardy, and F. J. Rich (1980), Effects of high-latitude conductivity on observed convection electric fields and Birkeland currents, *J. Geophys. Res.*, **85**, 6811.
- Song, Y., and R. L. Lysak (2000), Paradigm transition in cosmic physics, magnetic reconnection and the generation of field-aligned currents, in *Magnetospheric Current Systems*, edited by S.-I. Akasofu et al., p. 11, AGU, Washington, D.C.
- Tsyganenko, N. A., and D. P. Stern (1996), Modeling the global magnetic field of the large-scale Birkeland current systems, *J. Geophys. Res.*, **101**, 27,187.
- Vasyliunas, V. M. (1970), Mathematical models of magnetospheric convection and its coupling to the ionosphere, in *Particles and Fields in the Magnetosphere*, edited by B. M. McCormac, p. 60, D. Reidel, Norwell, Mass.
- Wallis, D. D., and E. E. Budzinski (1981), Empirical models of height integrated conductivities, *J. Geophys. Res.*, **86**, 125.
- Wilson, G. R., W. J. Burke, N. C. Maynard, C. Y. Huang, and H. J. Singer (2001), Global electrodynamics observed during the Initial and main phases of the July 1991 magnetic storm, *J. Geophys. Res.*, **106**, 24,517.
- Wing, S., and P. T. Newell (1998), Central plasma sheet ion properties as inferred from ionospheric observations, *J. Geophys. Res.*, **103**, 6785.
- Wing, S., and P. T. Newell (2000), Quiet time plasma sheet ion pressure contribution to Birkeland current, *J. Geophys. Res.*, **105**, 7793.
- Winningham, J. D., and W. J. Heikkila (1974), Polar cap auroral electron fluxes observed with Isis 1, *J. Geophys. Res.*, **79**, 949.
- Winningham, J. D., F. Yasuhara, S.-I. Akasofu, and W. J. Heikkila (1975), The latitudinal morphology of 10-eV to 10-keV electron fluxes during magnetically quiet and disturbed times in the 2100–0300 MLT sector, *J. Geophys. Res.*, **80**, 3148.

W. J. Burke, Space Vehicles Directorate, Air Force Research Laboratory, Hanscom Air Force Base, MA 01731, USA. (william.burke2@hanscom.af.mil)

C. Y. Huang, Institute for Scientific Research, Boston College, 402 St. Clement's Hall, 140 Commonwealth Avenue, Chestnut Hill, MA 02467-3862, USA. (cheryl.huang@hanscom.af.mil)



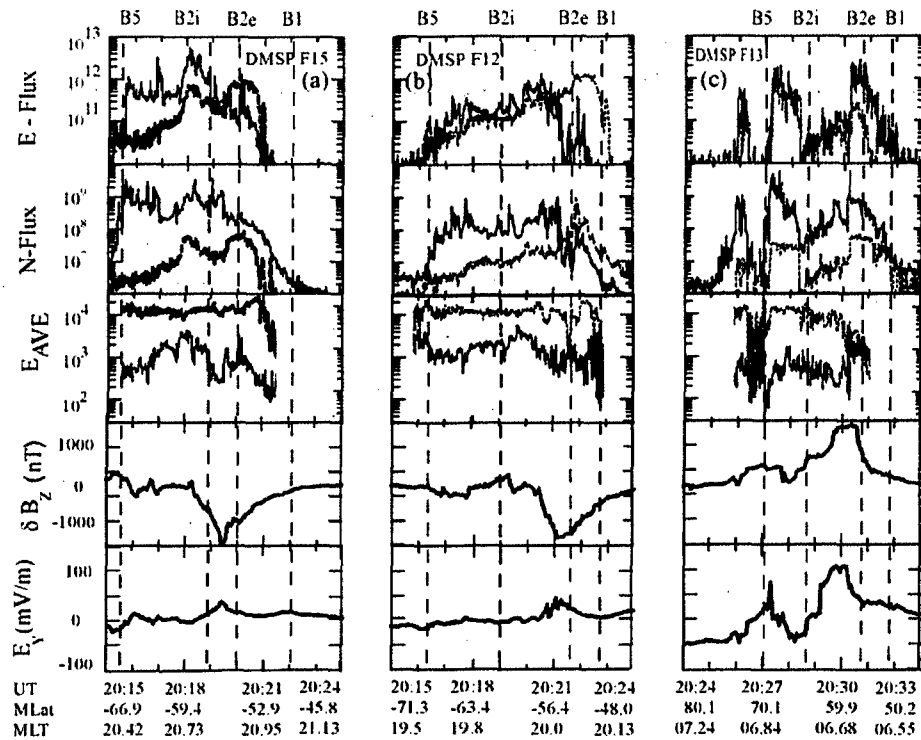


**Figure 5.** Particle and field measurements by (a) DMSP F15 and (b) F12 in the evening sector after 2015 UT, and (c) F13 in the morning sector after 2024 UT on 6 April 2000. From top to bottom the panels for each satellite show: (1) directional energy flux (E-Flux) in  $\text{eV cm}^{-2} \text{s}^{-1} \text{sr}^{-1}$  of down-coming electrons (upper line) and ions (lower line); (2) directional number fluxes (N-Flux) of down-coming electrons (upper line) and ions (bottom line) with energies between 30 eV and 30 keV, in  $\text{cm}^{-2} \text{s}^{-1} \text{sr}^{-1}$ ; (3) average energy of precipitating ions (upper line) and electrons (lower line), defined as  $E_{\text{AVE}} = E\text{-Flux}/N\text{-Flux}$ ; (4) the cross-track component of the magnetic field  $\delta B_z$  in nanotesla; and (5) the in-track component of the electric field  $E_y$  calculated from the observed ion drift and IGRF magnetic field values [Rich and Hairston, 1994]. Vertical dashed lines indicate times when the DMSP satellites crossed B1, B2e, B2i, and B5 [Newell et al., 1996]. Data are plotted as functions of UT, MLat, and MLT.

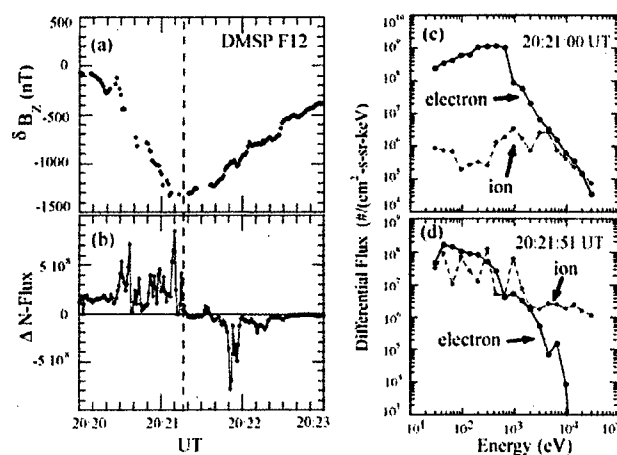


**Figure 6.** Particle and field characteristics of the FAC sheets crossed by DMSP F12 between 2020 and 2023 UT on 6 April 2000. Panels show (a) variations of  $\delta B_z$  and (b) differences between electron and ion number fluxes as a function of UT, as well as 5-s averaged ion and electron spectra measured by SSJ4 within the (c) upward and (d) downward FAC sheets.

<b>REPORT DOCUMENTATION PAGE</b>				Form Approved OMB No. 0704-0188	
Public reporting burden for this collection of information is estimated to average 1 hour per response, including the time for reviewing instructions, searching existing data sources, gathering and maintaining the data needed, and completing and reviewing this collection of information. Send comments regarding this burden estimate or any other aspect of this collection of information, including suggestions for reducing this burden to Department of Defense, Washington Headquarters Services, Directorate for Information Operations and Reports (0704-0188), 1215 Jefferson Davis Highway, Suite 1204, Arlington, VA 22202-4302. Respondents should be aware that notwithstanding any other provision of law, no person shall be subject to any penalty for failing to comply with a collection of information if it does not display a currently valid OMB control number. PLEASE DO NOT RETURN YOUR FORM TO THE ABOVE ADDRESS.					
<b>1. REPORT DATE (DD-MM-YYYY)</b> 13-06-2005		REPRINT			
<b>4. TITLE AND SUBTITLE</b> Transient Sheets of Field-Aligned Current Observed by DMSP During the Main Phase of a Magnetic Superstorm				<b>5a. CONTRACT NUMBER</b>	
				<b>5b. GRANT NUMBER</b>	
				<b>5c. PROGRAM ELEMENT NUMBER</b> 61102F	
<b>6. AUTHOR(S)</b> C. Y. Huang* and W.J. Burke				<b>5d. PROJECT NUMBER</b> 2311	
				<b>5e. TASK NUMBER</b> SD	
				<b>5f. WORK UNIT NUMBER</b> A3	
<b>7. PERFORMING ORGANIZATION NAME(S) AND ADDRESS(ES)</b> Air Force Research Laboratory/VSBXP 29 Randolph Road Hanscom AFB MA 01731-3010				<b>8. PERFORMING ORGANIZATION REPORT NUMBER</b>  AFRL-VS-HA-TR-2005-1063	
<b>9. SPONSORING / MONITORING AGENCY NAME(S) AND ADDRESS(ES)</b>				<b>10. SPONSOR/MONITOR'S ACRONYM(S)</b>	
				<b>11. SPONSOR/MONITOR'S REPORT NUMBER(S)</b>	
<b>12. DISTRIBUTION / AVAILABILITY STATEMENT</b> Approved for Public Release; Distribution Unlimited.  *Boston College, Institute for Scientific Research, Chestnut Hill, MA					
<b>13. SUPPLEMENTARY NOTES</b> REPRINTED FROM: JOURNAL OF GEOPHYSICAL RESEARCH, Vol 109, A06303, doi: 10.1029/2003JA010067, 2004.					
<b>14. ABSTRACT</b>  [1] During the main phase of the 6 April 2000 magnetic storm with $Dst \cong -300$ nT, four Defense Meteorological Satellite Program (DMSP) satellites encountered intense sheets of field-aligned currents (FACs). Their magnetic perturbations were $>1300$ nT, corresponding to integrated currents $ J_{  }  > 1$ A/m. The FACs appeared in both the evening and dawn magnetic local time sectors. They had relatively fast rise times ( $\sim 5$ min), lasted for $\sim 0.5$ hours, and were associated with widespread reconfigurations of plasma in the near-Earth magnetotail. The largest magnetic and related electric field perturbations occurred at magnetic latitudes $< 60^\circ$ . Magnetometer measurements from DMSP satellites show repeated episodes of similarly large FACs late in the main phase of this and other superstorms. Poynting flux calculations indicate that a few percent of the total ring current energy is dissipated as Joule heat in the midlatitude ionosphere during each of these events.					
<b>15. SUBJECT TERMS</b> Ionosphere/magnetosphere interactions      Energetic particles Field aligned currents      Superstorms      DMSP      Measured conductances					
<b>16. SECURITY CLASSIFICATION OF:</b>			<b>17. LIMITATION OF ABSTRACT</b>	<b>18. NUMBER OF PAGES</b>	<b>19a. NAME OF RESPONSIBLE PERSON</b>
<b>a. REPORT</b> UNCLAS	<b>b. THIS PAGE</b> UNCLAS	<b>c. THIS PAGE</b> UNCLAS	SAR		W. Burke
			<b>19b. TELEPHONE NUMBER (include area code)</b> 781-377-3980		